

**Title:** Combinatorial deployment of F-actin regulators to build complex 3D actin structures *in vivo*

**Authors:** Yi Xie<sup>1</sup> and J. Todd Blankenship<sup>1\*</sup>

**Affiliations:**

<sup>1</sup> Department of Biological Sciences, University of Denver, Denver, CO 80208, USA.

\* Author for correspondence (email: [todd.blankenship@du.edu](mailto:todd.blankenship@du.edu))

Lead contact: Todd Blankenship

**Keywords (4-10):** syncytial development; actin cortex; apical topologies; morphogenesis; actin regulation

# SUMMARY

Despite extensive studies on the actin regulators that direct microfilament dynamics, how these regulators are combinatorially utilized in organismal tissues to generate 3D structures is an unresolved question. Here, we present an in-depth characterization of cortical actin cap dynamics and their regulation *in vivo*. We identify rapid phases of initiation, expansion, duplication and disassembly and examine the functions of 7 different Actin and/or Nucleator Regulators (ANRPs) in guiding these behaviors. We find ANRPs provide distinct but cooperative activities in building actin cap morphologies – specifically, while DPod1 is a major regulator of actin intensities, Cortactin is required for continued cortical growth, while Coronin functions in both growth and intensity and is required for Cortactin localization to the cap periphery. Unexpectedly, cortical actin populations recover *more rapidly* after regulator disruption, suggestive of a potential deep competition for limited G-actin pools, and we measure *in vivo* Arp2/3 recruitment efficiencies through an ectopic relocalization strategy. Our results illustrate how the coordination of multiple actin regulators can orchestrate organized and dynamic actin structures in an *in vivo* system.

## INTRODUCTION

The mechanisms by which complex actin-based structures form are essential to shaping cell and tissue morphologies. This capacity to rapidly direct filamentous actin assembly is key to a cell's ability to either maintain or abruptly distort its cell shape. During development, the rapid changes in tissue morphologies are often a result of the remodeling of cortical actin and myosin activities (reviewed in Munjal and Lecuit, 2014; Heer and Martin, 2017). In keeping with this importance of regulating actin structures to achieve discrete cell shapes, a multitude of actin regulators are present within the genomes of eukaryotic animals (Siripala and Welch, 2007; Swaney and Li, 2016; Pegoraro et al., 2017). Some of the foremost examples of actin regulators are the nucleation and assembly complexes of the Formin and Arp2/3 complex families. Additionally, there are a host of actin and nucleator regulatory proteins present in the genomes of most higher animals (Siripala and Welch, 2007). However, although the biochemical activities of a broad array of actin regulators have been examined *in vitro*, how these combined activities are utilized by development *in vivo* to generate three-dimensional structures is less clear. Additionally, many actin regulators have been implicated in a variety of different processes ranging from the control of filament branching and turnover to the direct regulation and stabilization of nucleator complex function. Thus, the baseline effects of how these proteins contribute to building cortical structures is unclear. Here, we will examine the *in vivo* function of 7 major families of actin and/or nucleator regulatory proteins (ANRPs – DPod1, Coronin, Cortactin, Scar, Wasp, Wash, Carmil) in an intact organismal tissue context. We are using the highly-dynamic furrowing processes in the early syncytial fly embryo to study the rapid formation and disassembly of apical, cortical actin networks. In the end, the combined activities of different actin regulatory pathways must drive the cell shaping events necessary for development and the generation of a wide array of cell morphologies.

The *Drosophila* syncytium has a series of rapid transient cleavage cycles that are driven by actin polymerization and membrane trafficking pathways (Foe et al., 2000; Riggs et al., 2003; Pelissier et al., 2003; Grosshans et al., 2005; Yan et al., 2013; Holly et al., 2015; Mavor et al., 2016; Xie et al., 2018; Zhang et al., 2018). Following fertilization and the fusion of the male and female pronuclei, the zygotic nucleus undergoes thirteen rounds of replication in the absence of cell division to generate a single-celled embryo with approximately 5,000 nuclei (Hartenstein, 1993; Mazumdar and Mazumdar, 2002; Schmidt and Grosshans, 2018). The first nine rounds of replication occur deep in the yolk of the embryo; however, at cycle 10, nuclei migrate to the periphery and begin organizing the formation of cortical actin structures at the apical surface (apical F-actin caps) that will then seed the formation of cytokinetic-like furrows that serve to separate mitotic spindles in the syncytium.

These apical actin cap and cleavage furrow behaviors are transient, forming during each syncytial cell cycle where they compartmentalize and anchor mitotic spindles, before then regressing (Foe and Alberts, 1983; Sullivan et al., 1993; Cao et al., 2010; Holly et al., 2015). Embryos undergo four rapid rounds of actin cap and furrow formation (cycles 10-13), followed by a final fifth round of furrow ingression which results in the permanent packaging of nuclei into individual cells and the formation of an epithelium through a process known as cellularization. The ability to form these apical actin caps and ingressing furrows is essential to genomic stability – when these morphogenetic processes are disrupted, chromosomal segregation defects occur (Sullivan et al., 1993, Holly et al., 2015; Xie et al., 2018). Cap failure leads to aneuploid and polyploid nuclei, and defective nuclei are subsequently jettisoned into the deep yolk layer where they do not contribute further to gastrulation and epithelial development. This illustrates the importance of effective cortical actin caps and furrow function in the early embryo. These cleavage cycles of actin and furrow formation are exceptionally rapid, with each full round of cap assembly and disassembly occurring within 7 (cycle 10) to 20 minutes (cycle 13). F-actin regulation is therefore very dynamic,



and these stages represent an intriguing system to analyze how three-dimensional forms can be rapidly generated.

Here, we use 4D live-imaging of filamentous actin to determine phasic behaviors during cortical cap formation. Formation of these actin structures progresses through rapid periods encompassing exponential growth, stabilization, elongation and remodeling activities. Formin and Arp2/3 networks are responsible for building these cortical structures, and individual ANRPs have distinct functions in guiding cap growth and cap-associated actin intensities. We also generate an ANRP-related toolkit of genomic transgenes for these actin regulators and employ a mito-tag strategy to assess the strength of Arp2/3 nucleator recruitment *in vivo*. Finally, we explore how the disruption of ANRPs leads to *faster* actin network recoveries, which may be suggestive of a competition for a limited G-actin pool that controls actin assembly dynamics in the embryo.

# RESULTS

## Rapid formation and dissolution of apical actin cap structures

The apical actin caps in the early syncytial *Drosophila* embryo are highly-active structures that undergo cyclic behaviors of formation and disassembly on relatively short timescales. As such, they represent a unique opportunity to unravel the mechanisms that guide formation of complex three-dimensional actin-based structures. As a starting point, we live-imaged wild-type actin caps by labeling filamentous actin with an actin-binding domain construct derived from moesin (mCh:MoeABD). This method of labeling has been used extensively in the *Drosophila* embryo, and well-represents endogenous filamentous actin dynamics while avoiding problems that occur when fluorescent proteins are directly attached to actin or other labeling paradigms (such as Lifeact; Kiehart et al., 2000; Blankenship et al., 2006; Spracklen et al., 2014) (Fig. S1A-C, Fig. S2A-C). Actin cap formation was imaged through the four cycles that occur in the syncytial blastoderm (nuclear cycles of 10-13) and actin growth behaviors were analyzed (Fig. 1A, Fig. S3A-D).

Our results show that apical actin caps are exceptionally dynamic with an initial period of rapid exponential growth (~6-fold growth). During this phase, the major increase in cap dimensions occurs in as little as 120 seconds (Fig. 1A-C; Fig. S3). This is followed by cap stabilization and cap elongation, which correlates with spindle duplication and separation (Fig. 1A-C; Cao et al., 2010). Lastly, caps disassemble and then reform as small proto-caps around two central hubs to begin the next cycle of cap behaviors (Fig. 1A,B; Fig. S1A,B). In each cycle, the cap dynamics share similar features; as a result, we will focus on cycle 11 caps going forward (Fig. S3A-D).

During the expansion phase, cycle 11 actin caps rapidly expand from small proto-caps to caps 15-18 $\mu$ m in diameter and 206  $\mu$ m<sup>2</sup> in area within two minutes (Fig. 1A-F). Apical cap size

increases almost 6-fold during this period and growth rates peak early during expansion (Fig. 1E,F). Interestingly, despite the exponential growth in cap size, actin intensity increases only mildly, with a ~20% increase by the end of stabilization (Fig. 1G). This suggests that actin recruitment is carefully regulated spatially such that the cap grows exponentially but regional intensities do not.

The following stabilization phase lasts for ~60 seconds with caps largely maintaining their size. As the cell cycle continues, caps elongate and slightly increase in size (Fig. 1A-F). However, cap intensities begin to decrease and heterogeneity within the cap drops by ~one quarter of the maximum at the end of stabilization phase (Fig. 1G-I). Interestingly, the morphology of the cap during elongation switches from round to an elongated doughnut-like structure and loses intensity in internal actin populations (Fig. 1A). As the cell cycle reaches mitosis and chromosomal segregation, the caps begin to fragment and disassemble. Overall cap area begins to decline as F-actin gradually disbands leaving low intensity gaps in the middle of the elongating figure and along cap edges (Fig. 1A; Fig. S1A). During actin cap disassembly, the average intensity of caps drops, as well as the measured heterogeneity (Fig. 1G-I). These results demonstrate that the apical cap is a highly dynamic and complex F-actin structures, providing a good model for the investigation of the F-actin regulation *in vivo*.

### **Diaphanous and Arp2/3 networks direct actin cap dynamics**

After describing the filamentous actin dynamics above, we wanted to examine the major actin networks that drive these behaviors. The Formin Diaphanous as well as the Arp2/3 complex have been previously implicated in regulating actin nucleation at these syncytial stages (Stevenson et al., 2002; Zallen et al., 2002; Grosshans et al., 2005; Cao et al., 2010; Zhang et al., 2018).

According to published literature, Diaphanous appears to be the major regulator of furrow-associated F-actin, while Arp2/3 has been implicated in apical actin formation (Grosshans et al., 2005; Cao et al., 2010; Zhang et al., 2018), although comprehensive time-lapse based quantitation has been lacking. We therefore performed our own quantitative analysis of these protein's function in the early syncytial stages. Consistent with previous results, disruption of Diaphanous function deeply affects furrow-associated actin (Fig. S4). However, Diaphanous also shows a significant contribution to the early expansion of actin caps. *Dia* disrupted embryos have a ~35% reduction in cap area expansion, but a relatively mild 18% reduction in actin intensities and cap expansion rate (Fig 2A-H). We then examined the contribution of the Arp2/3 complex to actin behaviors. By contrast to Diaphanous, when Arp2/3 function is compromised there is an almost complete absence of cap expansion and cap actin intensities are reduced to 47% of wild-type levels (Fig 2A-H). Interestingly, the remaining actin structure appear to be hollowed out and missing internal actin populations (Fig 2A,B). These results show that Diaphanous and Arp2/3 both contribute to structuring apical actin caps, but that Arp2/3 is the major regulator of actin intensities and cap growth. The hollowed out internal cap structures as well as the failure in cap expansion also suggests a possible model in which Arp2/3 polymerizes F-actin internally, and the cap possesses a dispersion mechanism that flows F-actin filaments towards the edges so as to maintain consistent internal F-actin intensities.

## **Different ANRPs have distinct roles in building apical actin structures**

Given the above rapid dynamics of cap formation and nucleator function, we wanted to identify how actin and/or nucleator regulatory proteins (ANRPs) are deployed to control actin activities spatiotemporally in the construction of cortical actin caps. Extensive work across a variety of systems has revealed a diverse array of actin regulatory proteins, many of which have also been

implicated, to varying degrees, in controlling Arp2/3 activity or stability, although additional actin-related functions for these proteins likely exist (Siripala and Welch, 2007; Swaney and Li, 2016). Here we are focusing on seven of these families of proteins (DPod1, Coronin, Cortactin, Scar, Carmil, Wasp and Wash) – each of these families are represented within the *Drosophila* genome by single orthologs (Fig. 3A). Cortactin and Carmil have been shown to regulate Arp2/3 complex function as well as branch point stability (Cortactin) or filament capping (Carmil), and Scar/Wash/Wasp super-family proteins are known potent activators of Arp2/3 nucleation (Jung et al., 2001; Uruno et al., 2001; Weaver et al., 2001; Ammer and Weed, 2008; Pollitt and Insall, 2009). Scar has previously been suggested to be the most relevant member regulating Arp2/3 function in the early embryo, although this has not been tested systematically (Zallen et al., 2002; Levayer et al., 2011). *Drosophila* DPod1 contains WD40 domains and has similarity to Coronin-family proteins, which have been implicated in recruiting Arp2/3 complexes in the presence of preexisting actin filaments, as well as regulating cofilin function (Ghandi and Goode, 2008). Given the many associated functions of the ANRPs, we wanted to determine their baseline behaviors in regulating *in vivo* actin structures, and therefore analyzed actin cap dynamics in embryos compromised for each of these ANRPs (Fig. 3B).

Interestingly, these results identify distinct functions for Cortactin, DPod1, Coronin, and Scar in building F-actin caps (Fig. 3D-K), while disrupting Carmil, Wasp and Wash had little effect on caps (Fig. 3L,M; Fig. S5D-G). Compromising Coronin function causes an immediate defect in the expansion phase of cap formation (Fig. 3G,G'), with actin intensities at ~70% of control levels (Fig. 3C,F,G''). By contrast, disrupting DPod1 function produces caps that expand at near wild-type levels and possess wild-type areas until they fail to maintain area size in the later stages of apical cap function (Fig. 3E,E'). However, these embryos have dramatically reduced actin intensities throughout the cap area (Fig. 3E''). In embryos with compromised Cortactin function, there is a normal burst of actin expansion, but after ~120 seconds actin caps do not continue to grow and

steadily diminish in size, suggesting a role for Cortactin in growth at the cap periphery (Fig. 3H, I-I'). Interestingly, F-actin intensities within the smaller cap are at *higher* levels than control embryos (Fig. 3I'). Disrupting Scar function produces actin caps that show an early depletion of F-actin intensities followed by a delayed expansion phase in which the caps cannot fully reach control cap areas (Fig. 3J, K-K').

Given these effects on the size, shape, and intensity of apical actin caps, and our results demonstrating that the Arp2/3 complex is the major regulator of actin behaviors in the apical cortex, we next determined the degree to which Arp2/3 complex recruitment (as proxied by an endogenous Arp3:GFP) to the apical cortex was compromised in these various backgrounds. Disrupting the Formin Diaphanous had no effect on Arp3:GFP localization at apical structures (Fig. 3N,O). By contrast, disruption of ArpC4, one of the Arp2/3 complex subunits, almost completely abolishes apical Arp3:GFP localization and intensity (Fig. 3N,O). Interestingly, DPod1, which had the deepest impact on overall F-actin intensities, also had the largest effect on Arp3:GFP localization, while Coronin, Scar and Cortactin showed intermediate Arp3:GFP recruitment defects. Together, these results reveal distinct functions for individual ANRPs, with DPod1 being required for overall actin intensities, while Cortactin and Scar are necessary for cap expansion and maintenance. These results are also consistent with Coronin having an early function, possibly in the cap center, and Cortactin/Scar possessing a later function in controlling cap growth and maintenance of cap areas at the periphery. Coronin and Scar have both intensity (at early phases) and cap size functions, and Carmil, Wasp, and Wash have either minor or no contributions to cap dynamics.

### **Coronin directs Cortactin localization to the cap periphery**

To examine the expression and localization of the ANRPs during cap formation, we first used qPCR to examine the relative mRNA levels of each ANRP in the early syncytium. These results show that Coronin, Cortactin and DPod1 are highly expressed and Carmil and Wash are present at lower levels during syncytial stages (Fig. S6G). Dia, Wasp and Scar have intermediate expression. To further investigate the localization of each regulator, we generated an ANRP toolkit of expression constructs. We first generated either N- or C-terminal UAS GFP expression transgenic constructs (and in many cases, both N- and C- terminal; Table 1), and then followed up with either CRISPR/Cas9-mediated homologous recombination to knock-in GFP at endogenous loci or generated antibodies to examine endogenous localization. A CRISPR-generated GFP knock-in at the endogenous Arp3 locus shows a strong localization to the apical cap with little localization to furrows, consistent with our functional data (Fig. 3N; Fig. S6A). By contrast, neither UAS-driven Carmil nor Wasp localize to apical actin caps (Fig. 4E; Fig. S6E), again consistent with our conclusions from the functional analysis indicating they have little impact on apical cap dynamics. UAS-driven Coronin, Cortactin, Scar, and DPod1 all show varying degrees of localization to the actin caps (Fig. 4A-D), with endogenous CRISPR constructs or antibody stains showing similar patterns (Fig. S6B-D). One intriguing facet of these regulators' localization, however, is that Coronin and Cortactin display a complementary localization in mature caps, with Cortactin enrichment occurring at the cap periphery while Coronin possesses an enrichment in the cap interior (temporal overlays in Fig. 4F-I). This is also consistent with our functional analysis, in which Cortactin was required for cap growth late in the exponential phase and during later size maintenance, while Coronin was required for early cap growth. Additionally, the complementary localization suggested a possible antagonism between Coronin and Cortactin. To examine this, we imaged GFP:Cortactin embryos when Coronin was disrupted. Remarkably, this revealed that, in the absence of Coronin function, Cortactin fails to transition to the cap periphery, consistent with Coronin contributing to the ability of Cortactin to localize to the cell periphery to direct actin growth and the maintenance of cap edges (Fig. 4J,K).

## **Faster recovery of F-actin networks after ANRP disruption**

We next examined the dynamics of how actin networks in the early embryo form. To do so, we analyzed recovery rates after photobleaching. As a starting point, we measured recovery in cortical cap populations and in furrow-associated actin populations at ~120 seconds (when caps are approaching their early maximum in size) into cycle 11. These results revealed that actin is highly dynamic, with a halftime of recovery (T50) of only 8.2 seconds in the cap and a low immobile fraction of 17% (Fig. 5A-D). Furrow-associated actin is more stable with a T50 of 15.1 seconds (Fig. 5C). These recovery rates are nearly identical when actin is directly labeled with GFP, again demonstrating that tracking actin cap behaviors with the MoeABD:GFP accurately reflects actin dynamics (Fig. S2A-C).

We then measured recovery rates when the two major actin nucleating factors in the early embryo, Arp2/3 and Diaphanous, are disrupted. Our expectation was that as these networks are essential for cap growth and actin intensities, we would observe a longer recovery time after photobleaching. Surprisingly, we found that actin recovery is *much faster* when either Arp2/3 or Diaphanous function is disrupted. Indeed, although actin intensities are much reduced, the halftime to recovery of these intensities is nearly twice as fast as in wild-type embryo (4.2 s and 4.1 s in *ArpC4* and *Diaphanous shRNA* embryos, respectively; Fig. 5C). To examine this further, we analyzed what would happen to recovery rates when more actin is bound into stable filaments and less G-actin is available. We therefore injected embryos with low levels of jasplakinolide to stabilize F-actin – under these conditions, recovery rates increased (Fig. S7C-D). Similarly, reducing the G-actin availability by low-dose Latrunculin B injection also slowed recovery rates (Fig. S7C-D). Our data also addresses the relative stability of F-actin associated with the two networks, and suggests



that Diaphanous-associated actin is more stable than Arp2/3 filamentous actin, as the immobile fraction almost doubles when Diaphanous-mediated nucleation is the dominant regime in the actin cap (caps in which Arp2/3 function has been compromised). These results are intriguing, and at least two potential models could explain these behaviors: 1) the enhanced FRAP recovery rates are driven by increased rates of nucleation and polymerization due to higher free G-actin pools, or 2) higher FRAP recovery rates could be caused by increased actin turnover. Given that both Diaphanous and Arp2/3 complex function are deeply implicated in directing actin growth and nucleation, and the fact that they are chronically depleted in these experiments, we would suggest that these results support the first model and argues that these complexes are in a strong competition for a limited pool of available G-actin monomers.

Finally, we measured cap recovery rates when the individual ANRPs were disrupted. Similar to disrupting Arp2/3 or Dia function, compromising DPod1, Coronin, Cortactin, or Scar led to faster recovery rates, although to varying degrees (Fig. S7A-B). Interestingly, DPod1 disruption was almost comparable to disrupting Arp2/3 function in its effect on recovery rates and immobile fractions. This is consistent with our data indicating that DPod1 has the strongest impact on F-actin intensities in the cap. By analogy to the above, this could also suggest that actin intensities in the various disrupted backgrounds appear to well-reflect the degree to which specific actin networks are the predominant G-actin utilizing networks in the embryo.

### **Nucleator recruitment strengths of ANRP regulators**

As we have examined the localization and function of the different ANRPs in cortical cap formation, and as the Arp2/3 complex is the major regulator of new actin in the apical cortex, we wanted to test the strength of Arp2/3 recruitment by each ANRP *in vivo*. Although, as discussed above, the

ANRPs have been implicated in several different mechanisms of actin-regulation, many of the ANRPs have been shown to either activate or stabilize Arp2/3 complex function (Urano et al., 2001; Weaver et al., 2002; Uetrecht and Bear, 2006; Pollitt and Insall, 2009; Bhattacharya et al., 2016). We therefore adapted a mitochondrial-tagging assay (Wong and Munro, 2014) to recruit ANRPs to the mitochondria and then tested the degree to which Arp3 and F-actin become ectopically localized. Since DPod1, Cortactin, Coronin, and Scar had the strongest effects on actin cap formation, we fused each of these ANRPs to mCherry and an outer mitochondrial membrane mito-tag (Tom70-HA, 58 amino acids). Intriguingly, the mito-tagged ANRPs are each capable of recruiting Arp3:GFP, although to varying degrees (Fig. 6A-H). Further, they also appear able to activate Arp2/3 complex function, as filamentous actin is observed at the mito-tag puncta (Fig. S8B-E). To measure the strength of recruitment, we quantified the colocalization percentage and relative Arp3:GFP intensity as normalized to mito-ANRP:mCherry intensity. Of the tested ANRPs, mito-DPod1 possessed the strongest colocalization and recruitment ability (Fig. 6I-J). By contrast, Coronin had the lowest colocalization and recruitment ability while Cortactin and Scar had intermediate Arp3-recruiting activities (Fig. 6I-J). These results are consistent with our functional analysis which indicated that DPod1 is most important for overall actin cap intensities and suggest that a high potency ANRP, DPod1, has been selected to drive overall actin levels, while Coronin, Cortactin, and Scar largely have a spatial function in driving cap expansion. These results also provide some insight on the ANRPs relative potencies, as Cortactin demonstrates a high percent of colocalization, but relatively low recruitment ability, while Scar has moderate Arp3 colocalization but high recruitment ability (Fig. 6G-J).

### **ANRPs function for nuclear attachment**

Finally, we wanted to determine what the physiological impact of having cortical actin caps with different expansion rates, sizes and intensities would be on development. As F-actin caps have

been implicated in the apical anchorage and positioning of nuclei (Foe and Alberts, 1983; Sullivan et al., 1993; Blankenship and Wieschaus, 2001), we examined what the critical actin properties are that mediate nuclear anchorage against the substantial mitotic flows during division cycles. Loss of apical anchorage is readily apparent in Arp2/3 compromised embryos, with multiple nuclear fallout events being observed in a single cycle (Fig. 7A). In previous work, we have shown that a failure to properly segregate chromosomes led to aneuploid or polyploid nuclei and subsequent loss of apical nuclear positioning (Xie and Blankenship, 2018). However, here a different mechanism is at work, as we observed that nuclei that underwent apparently normal cell divisions still lost apical positioning in the Arp2/3 compromised background (Fig. 7A). We therefore correlated nuclear fallout with cortical cap properties such as intensity and cap expansion rates in the various ANRP backgrounds. This analysis revealed that the key property for nuclear anchorage was the growth in cap areas (Fig. 7B), while overall cap intensities had little correlation to nuclear fallout rates (Fig. 7C). These data suggest that cortical actin cap expansion and organization, as mediated by Cortactin, Coronin, and Scar, are essential for nuclear positioning and the maintenance of apical nuclear-cortex attachment sites.

# DISCUSSION

Cells have a variety of actin regulatory proteins to select from in the construction of cortical structures that support cell shape and function. Here, we used the early *Drosophila* syncytium as a system to study rapidly developing actin structures and tested the function of 7 different ANRP family members in directing specific properties of the apical cortex. We created an ANRP toolkit composed of 18 different transgenic constructs (Table 1) to analyze the interplay of actin regulators in an intact morphogenetic organism. This toolkit should form a useful reagent collection for the fly community, and has revealed that unique ANRPs were used to drive specific aspects of the growing actin cap. We observed that DPod1 has an essential function in supporting the overall actin intensities in the cap, but does not appear to function in directing the expansion of the actin cap. In contrast, Cortactin does not contribute to actin intensities, but plays a key role driving the continued growth and expansion of the cap. Interestingly, Coronin, which shares similar WD40 and DUF domain architectures to DPod1, has a dual role in supporting both actin intensity and cap growth. Coronin also shows the earliest function in directing cap growth, while Cortactin and Scar have cap growth rates that become compromised during the late portions of the exponential phase. Interestingly, our results also showed a potential cooperativity between Cortactin and Coronin that may underlie these early and late functions of the two regulatory proteins. Cortactin localizes to the cap periphery in later cortical caps, but fails to undergo this transition when Coronin function is disrupted. This suggests that centrally located Coronin may aid in directing Cortactin to a peripheral enrichment, and is consistent with a previous study showing a competition between Coronin and Cortactin in binding at actin branching points (Cai et al., 2008). These results are consistent with a combinatorial model for structuring the apical cortex in which DPod1 supports overall amounts of actin filaments, Coronin supports very early actin cap growth, and Cortactin and Scar promote mid-to-late cap growth and maintenance, although there are varying degrees of overlap in these functions.

We also comprehensively quantified apical actin dynamics when the major Formin and Arp2/3 actin networks are disrupted. Earlier works in the fly embryos suggested that the actin cap is largely dependent on Arp2/3 function, while the filamentous actin supporting ingressing furrows is largely Diaphanous/Formin driven (Grosshans et al., 2005; Cao et al., 2010; Zhang et al., 2018). Our results are broadly consistent with this viewpoint, although they also point to a lesser, but still substantial, Formin function in the cap as well. Interestingly, recent work has suggested that Formin proteins and Arp2/3 complex function possess an intriguing interplay in apical caps, with Diaphanous-based actin bundles being displaced by Arp2/3 actin nucleation function (Jiang and Harris, 2019). Our results also reveal a potential deep competition between the Diaphanous/Formin and Arp2/3 networks over the available G-actin pools. Somewhat surprisingly, actin fluorescent recovery rates were approximately twice as fast when either network was compromised. Although either increases in filament turnover or filament assembly could explain these faster recovery rates, the fact that chronic disruption of Diaphanous and Arp2/3 function (both of which are implicated in directing nucleation and filament growth) led to faster network recoveries is suggestive, to us, that this illustrates the degree to which G-actin availability limits filament assembly. It should be noted, however, that Coronin and DPod1 have each been implicated in regulating actin turnover, in addition to potential roles in regulating growth and nucleation (more on this below; Cai et al., 2008; Ghandi and Goode, 2008; Mikati et al., 2015). It also indicates that, even given the volume of the *Drosophila* embryo ( $9.02 \times 10^6 \mu\text{m}^3$ ; Markow et al., 2009) and the relatively few actin caps (~500-2000 caps during cycles 10-12) present in the early cortical cycles (i.e., per unit volume), local concentrations of G-actin still become limiting at the cortex.

To test the relative Arp2/3 recruiting potencies of the ANRPs, we chose to employ an ectopic relocation strategy (Wong and Munro, 2014). This mito-tag technique has the advantage of

testing factors in an intact tissue and cytoplasm, as opposed to artificially, buffered conditions *in vitro*. Interestingly, this revealed that DPod1 most potently recruited Arp2/3 to ectopic sites at the mitochondria, which correlates well with the importance of DPod1 for F-actin intensities at the cortical actin cap. Coronin had the weakest recruiting ability, possibly suggesting a primary role for Coronin in the regulation of Cortactin function and consistent with studies that suggest a complicated, and at times contradictory, function in Arp2/3 regulation (reviewed in Ghandi and Goode, 2008, discussed below). Interestingly, when Scar was found to colocalize with Arp3:GFP it was a very potent recruiter of Arp3/F-actin, but only a subset of mitochondrial Scar appeared active (~50% colocalization with Arp3:GFP). Embryos with disrupted DPod1, Cortactin, and Scar function also showed changes in actin stability and recovery rates (as indicated by immobile fractions and T50s) that mimicked the changes observed when Arp2/3 complex function was compromised. The partial colocalization of mito-tag Scar with Arp3:GFP additionally suggests a possible regulation and/or partial activation of Scar which may be limiting in terms of Scar function, and may explain why DPod1 is the most potent regulator of actin network function at these stages despite the similar strength with which Scar appears capable of recruiting Arp2/3 complex function. It may also be that this regulation is limiting in the relocation assay, and suggests one of the caveats to this approach (namely, that although this technique had the advantage of being *in vivo*, it still represents recruitment to an unnatural compartment that may have its own limitations imposed by the presence or absence of upstream signals and lipid bilayers). Nevertheless, this approach is a nicely complementary technique to *in vitro* biochemical measurements, and may provide a useful alternative approach for assaying protein recruitment abilities in the early fly embryo *in vivo*.

Finally, although much of our focus has been on the ANRPs in terms of guiding F-actin nucleation through the Arp2/3 complex, it should be pointed out that these regulators have been implicated in other actin-related processes (such as the control of filament branching and turnover) that may

be responsible for their relative effects on actin growth and intensities. Our functional results illustrate the final outcomes of disrupting ANRP function on actin morphologies, and, combined with the mito-tag assay, suggest the strength of Arp2/3-dependent regulation, but it is clear that several of these proteins have been implicated in additional biochemical processes other than Arp2/3 activation. For example, Coronin has been observed to both promote and inhibit Arp2/3 function, as well as directing F-actin turnover through cofilin/GMF function (Ghandi and Goode, 2008; Mikati et al., 2015). The Scar/Wasp/Wash family of proteins is typically viewed as directly activating Arp2/3 nucleating activities (reviewed in Molinie and Gautreau, 2018), and Cortactin can also activate nucleation at high concentrations, but additionally inhibits Arp2/3 debranching after nucleation has begun (Weaver et al., 2001; Uruno et al., 2001; Weaver et al., 2002; Cai et al., 2008). In other systems, Cortactin and Coronin have been found to compete in either stabilizing or destabilizing Arp2/3 branch points, and Cortactin is often preferentially found in newer filaments of migrating lamellipodia (Cai et al., 2008). It is tempting to speculate that this new-branch stabilizing function of Cortactin could be a reason why Cortactin has been selected to support the edge out-growth of the caps. Regardless of these varying activities, our results show the final products of these factors on the apical, cortical actin networks that form and position nuclei in the early fly embryo. It will be interesting in future experiments to begin to further examine the biochemical partners that may help mediate the activities observed in this study.

# **MATERIALS & METHODS**

## *Fly stock and genetics:*

All stocks were maintained at 25°C. Genotypes used in this study are listed in Table S1 and Table S2. To generate endogenous GFP reporter constructs, the CRISPR/Cas9 system was used to knock-in an N-terminal (downstream of ATG site) or C-terminal (upstream of stop codon) GFP tag through the use of a donor construct with 1kb or 1.5kb homologous sequences flanking GFP. The homology donors were constructed in pBluescript SK(-). The upstream and downstream guide RNAs were designed in flyCRISPR (<https://flycrispr.org/>) and inserted into pU6-BbsI-chiRNA. Genomic PAM sites were pre-verified by DNA sequencing to avoid single nucleotide polymorphisms present in different *Drosophila* lines. Donor constructs (500ng/μL) and guide RNA constructs (100ng/μL) were mixed and injected into nos-Cas9 expressing embryos (BestGene). Potential insertions were balanced, and flies were screened by genomic PCR (Platinum Taq DNA polymerase, Invitrogen) after genome extraction from larva or adults (E.Z.N.A insect DNA kit, Omega Biotek).

To generate UAS GFP-tagged fly stocks, N-terminal or C-terminal eGFP was inserted into pUASp or pUASt along with the coding sequence for a given gene. Mito-tagged constructs were made by inserting Tom70-HA (generous gift of S. Munro lab) at the N-terminus of mCh:ANRPs in pUASp. The constructs were injected into embryos (BestGene) for transgene recovery and balanced. UAS constructs were crossed to P[mat-tub-Gal4] mat67; P[mat-tub-Gal4] mat15 (mat 67; 15) maternal drivers for Gal4-driven expression. To knockdown gene function, shRNA lines were also crossed to mat-tub-Gal4 lines and females were recovered from either mat-67-Gal4; mat-15-Gal4 double Gal4 lines for high shRNA expression or to individual mat-67-Gal4 or mat-15-Gal4 for moderate shRNA expression.



*Microscopy and time-lapse imaging:*

Spinning-disk confocal microscopy was performed on a Zeiss/Solamere Technologies Group spinning-disk with a 63X 1.4NA objective lens (image stacks were acquired every 5s and were composed of 15 z-layers with 0.3µm z-steps), or Olympus Fluoview FV3000 confocal laser scanning microscope with 40X or 60X 1.35NA objective lens (images acquired every 5s at 12 ms/pixel exposure settings). Embryos were collected on yeasted apple juice agarose plates. After dechoriation in 50% bleach, embryos were transferred to an air-permeable membrane and mounted in Halocarbon 27 oil (Sigma). A coverslip was placed on embryos for live-imaging. For FRAP experiments, Olympus Fluoview FV3000 confocal laser scanning microscope with 40X or 60X 1.35NA objective lens was used. Images were acquired every 1s at 2 ms/pixel exposure settings. For drug injection, after dechoriation embryos were glued on a coverslip and dehydrated for 12-15min, covered in Halocarbon oil 700 (Sigma). Jasplakinolide (20µg/mL) and Latrunculin B (200nM) were injected into embryos, followed by regular imaging protocol for FRAP and live-imaging. MicroManager 1.4, FIJI/ImageJ, and Olympus Fluoview software were used for image collection and analysis. All movies were acquired at 25°C.

*Embryo fixation, antibodies, immunostaining and imaging:*

Dechorionated embryos were fixed at the interface of heptane and either 18.5% paraformaldehyde (Electron Microscopy Sciences) (Postner et al, 1994) for 30 minutes for actin cap staining, or 4% paraformaldehyde for 70 minutes for mito-tagged embryo staining, in 0.1 M sodium phosphate buffer (pH7.4). The embryos were manually devitellinized and stained with rabbit anti-GFP (1:1000, Invitrogen) and/or anti-dsRed(1:500, Invitrogen). Alexa 546 or 647-phalloidin (1:200, Invitrogen), or secondary antibodies conjugated with Alexa 488 or 568 (Invitrogen) were used at 1:500. Coronin peptide antibody was used at 1:100 dilution. Coronin peptide antibody was generated by GenScript as peptide-KLH conjugation in New Zealand rabbits (sequence in Table 3). The affinity-purified antibody were used at 1:100 dilution (~10µg/mL).

Embryos were mounted in ProLong Gold (Life Technologies). Olympus Fluoview FV3000 confocal laser scanning microscopy was used for immunostained embryos imaging. Exposure settings of 8 or 12 ms/pixel were used for image acquisition.

#### *Actin cap dynamics measurements:*

Apical cap dynamics were measured by live-imaging embryos with UAS:mCh:MoeABD marker. The measured apical cap region was determined by the region 0.9 $\mu$ m (3 z-planes) below the apical most layer in which the embryo could be detected. The apical cap area was selected based on the cap F-actin boundary after background subtraction. Area, average intensity, and standard deviation were quantified in FIJI/ImageJ. Normalized area measurements were done by normalizing to the cap size at cap initiation.

#### *Intensity measurements:*

For Arp3:GFP intensity measurements, a circular region (7705 px<sup>2</sup>, ~207  $\mu$ m<sup>2</sup>) was quantified in each cap with FIJI/ImageJ. For line intensity measurements, the intensity profiles were quantified in FIJI/ImageJ, and smoothed by averaging three neighboring points. For cap intensity measurements in FRAP experiments, the FRAP defined regions were measured for intensity in FIJI/ImageJ.

#### *Real-time PCR:*

shRNA lines were crossed to P[mat-tub-Gal4] mat67; P[mat-tub-Gal4] mat15. The F1 embryos were collected by standard protocol, shredded (QIAshredder, QIAGEN), and RNA extracted (Quick-RNA MicroPrep, Zymo Research). The RNA extracts were reverse transcribed (QuantiTech Reverse Transcription Kit, Invitrogen) and used for real-time PCR (QuantiTech SYBR Green RT-PCR, Invitrogen; Bio-Rad iQ5). The primers used for RT-PCR are listed in Table 3.

534

535 *Statistics and repeatability:*

536 A Shapiro-Wilk test was performed in OriginPro to test for statistical normality of data. Cap area,  
537 area change, expansion rate, intensity, heterogeneity and heterogeneity change data were tested  
538 for statistical significance using Student's t-test for all normal data. ns:  $p > 0.05$ ; \*:  $p < 0.05$ ; \*\*:  $p < 0.005$ ;  
539 \*\*\*:  $p < 0.0005$ . Each cycle 11 cap was measured for ~110 time points (every 5s), with  
540 all measurements being quantified from at least 9 individual caps from a minimum of 3 embryos.  
541 n represent the total number of individual structures measured, and N represent the total embryos  
542 tested.

543

544 *Image editing and figure preparation:*

545 Spinning disk and laser scanning confocal microscopy images were edited by FIJI/ImageJ and  
546 Adobe Photoshop. Images were uniformly leveled for optimal channel appearance except where  
547 noted. Actin cap curves (average values and errors), bar graphs (average values and errors), box  
548 & whisker plots (boxes as 25%-75% values, whiskers as minimal and maximal values, and lines  
549 in the boxes as median) and other graphs were made in OriginPro. Error bars are shown as S.E.M.  
550 Figures were prepared and labeled in Adobe Illustrator.

551

## References

- Ammer, A.G. and Weed, S.A., 2008. Cortactin Branches Out: Roles in Regulating Protrusive Actin Dynamics. *Cell Motility Cytoskeleton*, 65(9), pp.687–707.
- Bhattacharya, K., Swaminathan, K., Peche, V.S., Clemen, C.S., Knyphausen, P., Lammers, M., Noegel, A.A. and Rastetter, R.H., 2016. Novel Coronin7 interactions with Cdc42 and N-WASP regulate actin organization and Golgi morphology. *Scientific reports*, 6(1), pp.1-17.
- Blankenship, J.T. and Wieschaus, E., 2001. Two new roles for the Drosophila AP patterning system in early morphogenesis. *Development*, 128(24), pp.5129-5138.
- Blankenship, J.T., Backovic, S.T., Sanny, J.S., Weitz, O. and Zallen, J.A., 2006. Multicellular rosette formation links planar cell polarity to tissue morphogenesis. *Developmental cell*, 11(4), pp.459-470. <https://dx.doi.org/10.1016/j.devcel.2006.09.007>
- Cai, L., Makhov, A.M., Schafer, D.A. and Bear, J.E., 2008. Coronin 1B antagonizes cortactin and remodels Arp2/3-containing actin branches in lamellipodia. *Cell*, 134(5), pp.828-842. <https://dx.doi.org/10.1016/j.cell.2008.06.054>
- Cao, J., Crest, J., Fasulo, B. and Sullivan, W., 2010. Cortical actin dynamics facilitate early-stage centrosome separation. *Current Biology*, 20(8), pp.770-776. <https://dx.doi.org/10.1016/j.cub.2010.02.060>
- Edelstein, A.D., Tsuchida, M.A., Amodaj, N., Pinkard, H., Vale, R.D. and Stuurman, N., 2014. Advanced methods of microscope control using µManager software. *Journal of biological methods*, 1(2). <https://dx.doi.org/10.14440/jbm.2014.36>
- Farina, F., Gaillard, J., Guérin, C., Couté, Y., Sillibourne, J., Blanchoin, L. and Théry, M., 2016. The centrosome is an actin-organizing centre. *Nature cell biology*, 18(1), pp.65-75. <https://dx.doi.org/10.1038/ncb3285>
- Foe, V.E. and Alberts, B.M., 1983. Studies of nuclear and cytoplasmic behaviour during the five mitotic cycles that precede gastrulation in Drosophila embryogenesis. *Journal of cell science*, 61(1), pp.31-70.
- Foe, V.E., Field, C.M. and Odell, G.M., 2000. Microtubules and mitotic cycle phase modulate spatiotemporal distributions of F-actin and myosin II in Drosophila syncytial blastoderm embryos. *Development*, 127(9), pp.1767-1787.
- Gandhi, M. and Goode, B.L., 2008. Coronin: the double-edged sword of actin dynamics. In *The Coronin Family of Proteins* (pp. 72-87). Springer, New York, NY. [https://dx.doi.org/10.1007/978-0-387-09595-0\\_7](https://dx.doi.org/10.1007/978-0-387-09595-0_7)
- Großhans, J., Wenzl, C., Herz, H.M., Bartoszewski, S., Schnorrer, F., Vogt, N., Schwarz, H. and Müller, H.A., 2005. RhoGEF2 and the formin Dia control the formation of the furrow canal by directed actin assembly during Drosophila cellularisation. *Development*, 132(5), pp.1009-1020. <https://dx.doi.org/10.1242/dev.01669>
- Hartenstein, V., 1993. *Atlas of Drosophila development* (Vol. 328). Cold Spring Harbor Laboratory Press.
- Heer, N.C. and Martin, A.C., 2017. Tension, contraction and tissue morphogenesis. *Development*, 144(23), pp.4249-4260. <https://dx.doi.org/10.1242/dev.151282>
- Holly, R.M., Mavor, L.M., Zuo, Z. and Blankenship, J.T., 2015. A rapid, membrane-dependent pathway directs furrow formation through RalA in the early Drosophila embryo. *Development*, 142(13), pp.2316-2328. <https://dx.doi.org/10.1242/dev.120998>

Jiang, T. and Harris, T.J., 2019. Par-1 controls the composition and growth of cortical actin caps during *Drosophila* embryo cleavage. *Journal of Cell Biology*, 218(12), pp.4195-4214. <https://dx.doi.org/10.1083/jcb.201903152>

Jung, G., Remmert, K., Wu, X., Volosky, J.M. and Hammer, J.A., 2001. The Dictyostelium CARMIL Protein Links Capping Protein and the Arp2/3 Complex to Type I Myosins Through Their SH3 Domains. *Journal of Cell Biology*, 153(7), pp.1479-97.

Khatau, S.B., Kim, D.H., Hale, C.M., Bloom, R.J. and Wirtz, D., 2010. The perinuclear actin cap in health and disease. *Nucleus*, 1(4), pp.337-342. <https://dx.doi.org/10.4161/nucl.1.4.12331>

Kiehart, D.P., Galbraith, C.G., Edwards, K.A., Rickoll, W.L. and Montague, R.A., 2000. Multiple forces contribute to cell sheet morphogenesis for dorsal closure in *Drosophila*. *The Journal of cell biology*, 149(2), pp.471-490. <https://dx.doi.org/10.1083/jcb.149.2.471>

Levayer, R., Pelissier-Monier, A. and Lecuit, T., 2011. Spatial regulation of Dia and Myosin-II by RhoGEF2 controls initiation of E-cadherin endocytosis during epithelial morphogenesis. *Nature cell biology*, 13(5), pp.529-540. <https://dx.doi.org/10.1038/ncb2224>

Markow, T.A., Beall, S. and Matzkin, L.M., 2009. Egg size, embryonic development time and ovoviviparity in *Drosophila* species. *Journal of evolutionary biology*, 22(2), pp.430-434. <https://dx.doi.org/10.1111/j.1420-9101.2008.01649.x>

Mavor, L.M., Miao, H., Zuo, Z., Holly, R.M., Xie, Y., Loerke, D. and Blankenship, J.T., 2016. Rab8 directs furrow ingression and membrane addition during epithelial formation in *Drosophila melanogaster*. *Development*, 143(5), pp.892-903. <https://dx.doi.org/10.1242/dev.128876>

Mazumdar, A. and Mazumdar, M., 2002. How one becomes many: blastoderm cellularization in *Drosophila melanogaster*. *Bioessays*, 24(11), pp.1012-1022. <https://dx.doi.org/10.1002/bies.10184>

Mikati, M.A., Breitsprecher, D., Jansen, S., Reisler, E. and Goode, B.L., 2015. Coronin enhances actin filament severing by recruiting cofilin to filament sides and altering F-actin conformation. *Journal of molecular biology*, 427(19), pp.3137-3147. <https://dx.doi.org/10.1016/j.jmb.2015.08.011>

Molinie, N. and Gautreau, A., 2018. The Arp2/3 regulatory system and its deregulation in cancer. *Physiological reviews*, 98(1), pp.215-238. <https://dx.doi.org/10.1152/physrev.00006.2017>

Munjal, A. and Lecuit, T., 2014. Actomyosin networks and tissue morphogenesis. *Development*, 141(9), pp.1789-1793. <https://dx.doi.org/10.1242/dev.091645>

Pegoraro, A.F., Janmey, P. and Weitz, D.A., 2017. Mechanical properties of the cytoskeleton and cells. *Cold Spring Harbor perspectives in biology*, 9(11), p.a022038. <https://dx.doi.org/10.1101/cshperspect.a022038>

Pelissier, A., Chauvin, J.P. and Lecuit, T., 2003. Trafficking through Rab11 endosomes is required for cellularization during *Drosophila* embryogenesis. *Current biology*, 13(21), pp.1848-1857. <https://dx.doi.org/10.1016/j.cub.2003.10.023>

Pollitt, A.Y. and Insall, R.H., 2009. WASP and SCAR/WAVE proteins: the drivers of actin assembly. *Journal of cell science*, 122(15), pp.2575-2578.

Postner, M.A. and Wieschaus, E.F., 1994. The nullo protein is a component of the actin-myosin network that mediates cellularization in *Drosophila melanogaster* embryos. *Journal of Cell Science*, 107(7), pp.1863-1873.

- 662 Riggs, B., Rothwell, W., Mische, S., Hickson, G.R., Matheson, J., Hays, T.S., Gould, G.W. and Sullivan,  
663 W., 2003. Actin cytoskeleton remodeling during early *Drosophila* furrow formation requires recycling  
664 endosomal components Nuclear-fallout and Rab11. *The Journal of cell biology*, 163(1), pp.143-154.  
665 <https://dx.doi.org/10.1083/jcb.200305115>  
666
- 667 Schmidt, A. and Grosshans, J., 2018. Dynamics of cortical domains in early *Drosophila*  
668 development. *Journal of cell science*, 131(7). <https://dx.doi.org/10.1242/jcs.212795>  
669
- 670 Schindelin, J., Arganda-Carreras, I., Frise, E., Kaynig, V., Longair, M., Pietzsch, T., Preibisch, S.,  
671 Rueden, C., Saalfeld, S., Schmid, B. and Tinevez, J.Y., 2012. Fiji: an open-source platform for biological-  
672 image analysis. *Nature methods*, 9(7), pp.676-682. <https://doi.org/10.1038/nmeth.2019>  
673
- 674 Siripala, A.D. and Welch, M.D., 2007. SnapShot: actin regulators I. *Cell*, 128(3), pp.626-e1.  
675 <https://doi.org/10.1016/j.cell.2007.02.001>  
676
- 677 Spracklen, A.J., Fagan, T.N., Lovander, K.E. and Tootle, T.L., 2014. The pros and cons of common actin  
678 labeling tools for visualizing actin dynamics during *Drosophila* oogenesis. *Developmental biology*, 393(2),  
679 pp.209-226. <https://doi.org/10.1016/j.ydbio.2014.06.022>  
680
- 681 Stevenson, V., Hudson, A., Cooley, L. and Theurkauf, W.E., 2002. Arp2/3-dependent pseudocleavage  
682 furrow assembly in syncytial *Drosophila* embryos. *Current Biology*, 12(9), pp.705-711.  
683 [https://doi.org/10.1016/S0960-9822\(02\)00807-2](https://doi.org/10.1016/S0960-9822(02)00807-2)  
684
- 685 Sullivan, W., Daily, D.R., Fogarty, P., Yook, K.J. and Pimpinelli, S., 1993. Delays in anaphase initiation  
686 occur in individual nuclei of the syncytial *Drosophila* embryo. *Molecular biology of the cell*, 4(9), pp.885-  
687 896. <https://doi.org/10.1091/mbc.4.9.885>  
688
- 689 Swaney, K.F. and Li, R., 2016. Function and regulation of the Arp2/3 complex during cell migration in  
690 diverse environments. *Current opinion in cell biology*, 42, pp.63-72.  
691 <https://doi.org/10.1016/j.ceb.2016.04.005>  
692
- 693 Uetrecht, A.C. and Bear, J.E., 2006. Coronins: the return of the crown. *Trends in cell biology*, 16(8),  
694 pp.421-426.  
695
- 696 Uruno, T., Liu, J., Zhang, P., Fan, Y.X., Egile, C., Li, R., Mueller, S.C. and Zhan, X., 2001. Activation of  
697 Arp2/3 complex-mediated actin polymerization by cortactin. *Nature cell biology*, 3(3), pp.259-266.  
698 <https://doi.org/10.1038/35060051>  
699
- 700 Warn, R.M., 1986. The cytoskeleton of the early *Drosophila* embryo. *J Cell Sci*, 1986(Supplement 5),  
701 pp.311-328. [https://doi.org/10.1242/jcs.1986.supplement\\_5.20](https://doi.org/10.1242/jcs.1986.supplement_5.20)  
702
- 703 Weaver, A.M., Karginov, A.V., Kinley, A.W., Weed, S.A., Li, Y., Parsons, J.T. and Cooper, J.A., 2001.  
704 Cortactin promotes and stabilizes Arp2/3-induced actin filament network formation. *Current*  
705 *Biology*, 11(5), pp.370-374. [https://doi.org/10.1016/s0960-9822\(01\)00098-7](https://doi.org/10.1016/s0960-9822(01)00098-7)  
706
- 707 Weaver, A.M., Heuser, J.E., Karginov, A.V., Lee, W.L., Parsons, J.T. and Cooper, J.A., 2002. Interaction  
708 of cortactin and N-WASP with Arp2/3 complex. *Current Biology*, 12(15), pp.1270-1278.  
709 [https://doi.org/10.1016/s0960-9822\(02\)01035-7](https://doi.org/10.1016/s0960-9822(02)01035-7)  
710
- 711 Wong, M. and Munro, S., 2014. The specificity of vesicle traffic to the Golgi is encoded in the golgin  
712 coiled-coil proteins. *Science*, 346(6209), p.1256898. <https://doi.org/10.1126/science.1256898>  
713
- 714 Xie, Y. and Blankenship, J.T., 2018. Differentially-dimensioned furrow formation by zygotic gene  
715 expression and the MBT. *PLoS genetics*, 14(1), p.e1007174.  
716 <https://doi.org/10.1371/journal.pgen.1007174>  
717

- Yan, S., Lv, Z., Winterhoff, M., Wenzl, C., Zobel, T., Faix, J., Bogdan, S. and Grosshans, J., 2013. The F-BAR protein Cip4/Toca-1 antagonizes the formin Diaphanous in membrane stabilization and compartmentalization. *Journal of cell science*, 126(8), pp.1796-1805. <https://doi.org/10.1242/jcs.118422>
- Zallen, J.A., Cohen, Y., Hudson, A.M., Cooley, L., Wieschaus, E. and Schejter, E.D., 2002. SCAR is a primary regulator of Arp2/3-dependent morphological events in *Drosophila*. *The Journal of cell biology*, 156(4), pp.689-701. <https://doi.org/10.1083/jcb.200109057>
- Zhang, Y., Jessica, C.Y., Jiang, T., Fernandez-Gonzalez, R. and Harris, T.J., 2018. Collision of expanding actin caps with actomyosin borders for cortical bending and mitotic rounding in a syncytium. *Developmental cell*, 45(5), pp.551-564. <https://doi.org/10.1016/j.devcel.2018.04.024>



## FIGURES & FIGURE LEGENDS

### Figure 1

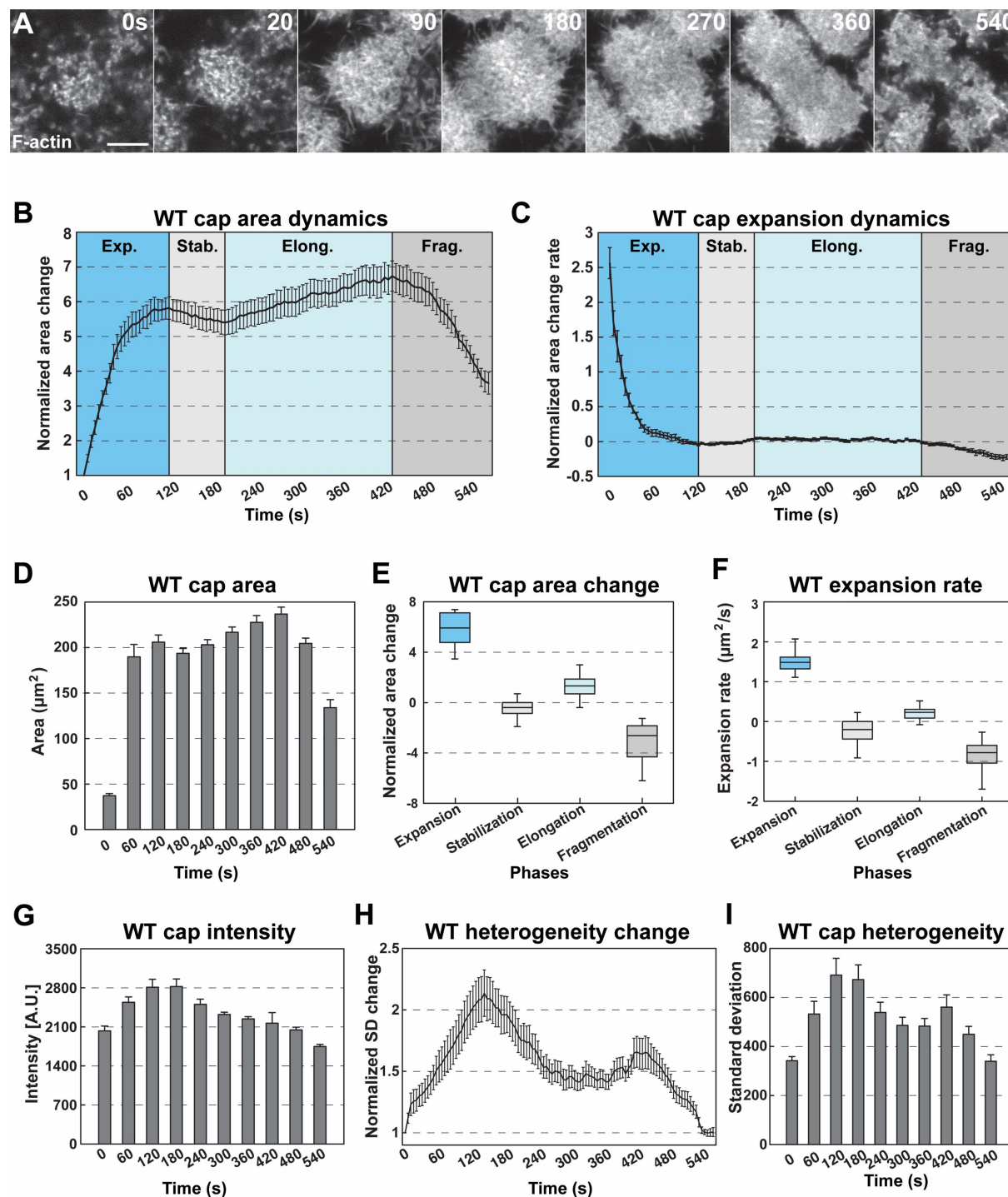


**Figure 1. Rapid formation and dissolution of cortical actin cap structures.** (A) Still images from live-imaging of apical F-actin dynamics (UAS:moeABD:mCherry, cycle 11) at  $t=0, 20, 90, 180, 270, 360, 540$ s. Scale bar= $5\mu\text{m}$ . (B) WT actin cap area dynamics from cycle 11 (measured cap  $n=15$ , from embryo  $N=4$ ). Cap areas are normalized to the size at  $t=0$ s. Four different phases are labeled (Exp.: Expansion; Stab.:



*Stabilization*; Elong.: *Elongation*; and Frag.: *Fragmentation* phases). (C) WT actin cap expansion rate from 30s rolling window (cycle 11, n=15, N=4). (D) WT actin cap area ( $\mu\text{m}^2$ ) from cycle 11 at t=0, 60, 120, 180, 240, 300, 360, 420, 480, 540s (n=15, N=4). (E) WT actin cap area change in different phases (cycle 11, n=15, N=4). The values are calculated by the cap area at the end point divided by the area at the beginning of each phase. (F) Average WT actin cap area expansion rate ( $\mu\text{m}^2/\text{s}$ ) in different phases (cycle 11, n=15, N=4). (G) Average WT actin cap intensity (A.U.) from cycle 11 at t=0, 60, 120, 180, 240, 300, 360, 420, 480, 540s (n=12, N=3). (H) WT actin cap heterogeneity dynamics from cycle 11 (n=15, N=4). The heterogeneity is measured as the intensity standard deviation normalized to the value at t=0s. (I) WT actin cap heterogeneity from cycle 11 at t=0, 60, 120, 180, 240, 300, 360, 420, 480, 540s (n=15, N=4).

**Figure 2**

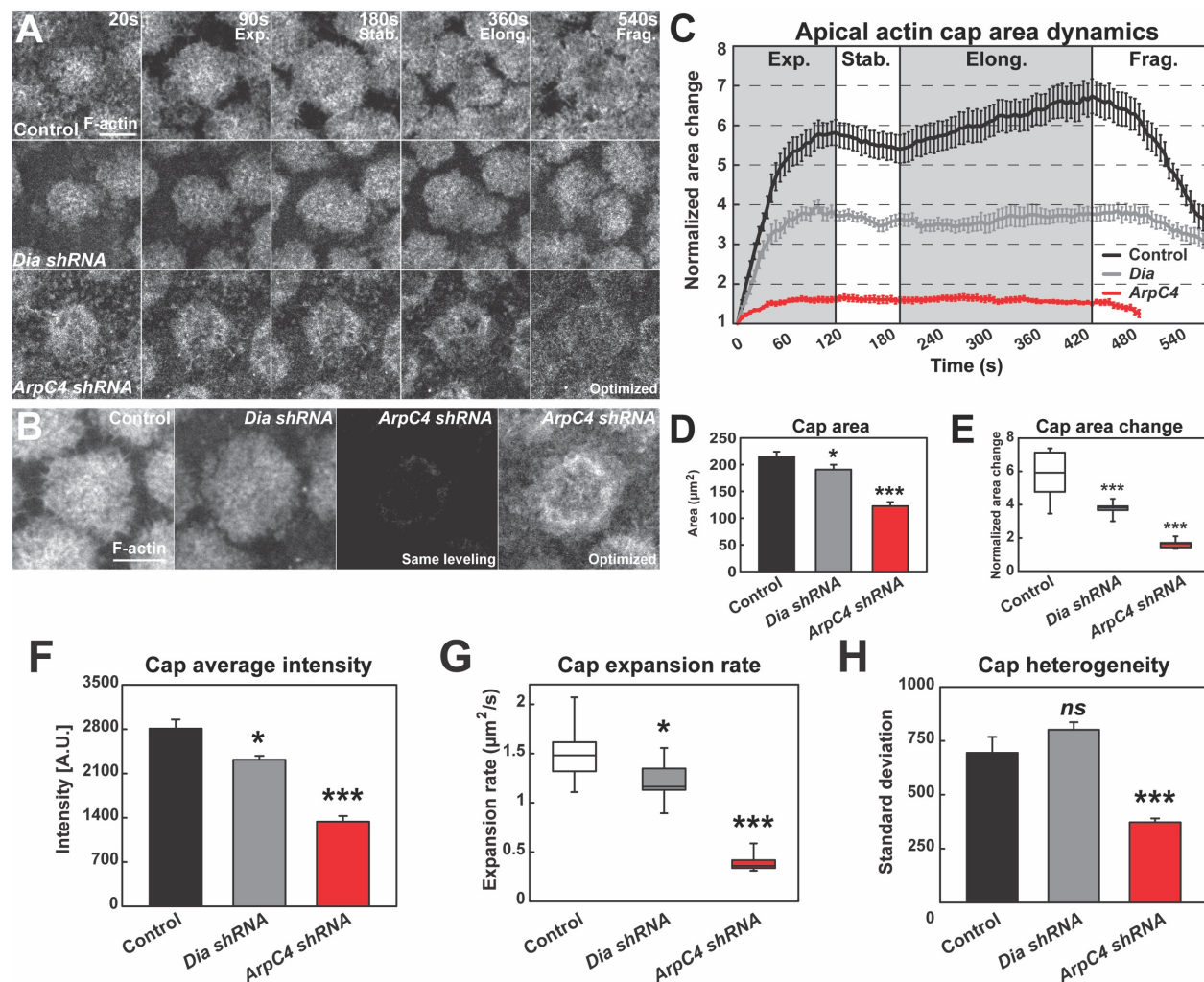
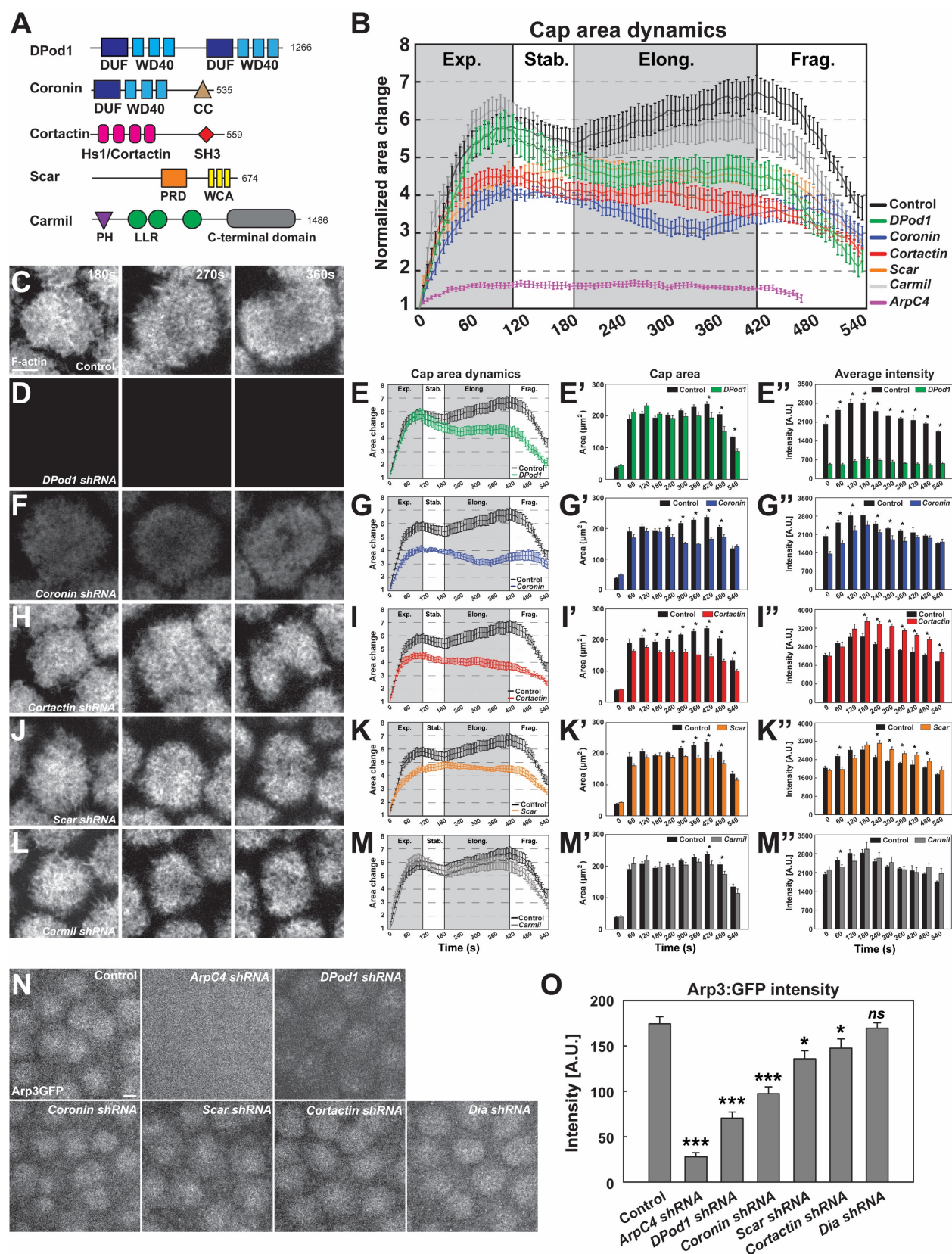


**Figure 2. Quantitative dynamics of Formin and Arp2/3-driven actin networks.** (A) Still images from live-imaging of apical F-actin dynamics (UAS:moeABD:mCherry, cycle 11) from control, *Dia shRNA* and *ArpC4 shRNA* lines at t=20, 90, 180, 360, 540s. Four different phases are labeled (Exp.: Expansion; Stab.: Stabilization; Elong.: Elongation; and Frag.: Fragmentation phases). Scale bar=5μm. (B) Still images showing F-actin cap intensities by live-imaging (UAS:moeABD:mCherry, cycle 11) from control, *Dia shRNA* and *ArpC4 shRNA* lines at t=120s. First 3 panels are leveled and imaged equivalently, with the last panel optimized for visualization. Scale bar=5μm. (C) Actin cap area dynamics of control (black, n=15, N=4), *Dia shRNA* (grey, n=10, N=3) and *ArpC4 shRNA* (red, n=11, N=3) from cycle 11. Cap areas are normalized to the size at t=0s. (D) Actin cap area (μm<sup>2</sup>) of control (n=15, N=4), *Dia shRNA* (n=10, N=3), and *ArpC4 shRNA* (n=11, N=3) at t=120s in cycle 11. \* p<0.05, \*\*\* p<0.0005. (E) Actin cap area change of control (n=15, N=4), *Dia shRNA* (n=10, N=3), and *ArpC4 shRNA* (n=11, N=3) from t=120s to t=0s in cycle 11. \*\*\* p<0.0005. (F) Average intensity of apical cap structures of control (n=12, N=3), *Dia shRNA* (n=10, N=3), and *ArpC4 shRNA* (n=11, N=3) at t=120s in cycle 11. \* p<0.05, \*\*\* p<0.0005. (G) Actin cap area expansion rate of control (n=15, N=4), *Dia shRNA* (n=10, N=3), and *ArpC4 shRNA* (n=11, N=3) from 0-120s in cycle 11. \* p<0.05, \*\*\* p<0.0005. (H) Actin cap heterogeneity (intensity standard deviation) of control (n=15, N=4), *Dia shRNA* (n=10, N=3), and *ArpC4 shRNA* (n=11, N=3) at t=120s in cycle 11. ns: not significant, \*\*\* p<0.0005.

**Figure 3**





777

778 **Figure 3. ANRPs have distinct roles in building cortical actin structures.** (A) Schematics of different  
779 ANRPs domain organization. Domains are collected from Flybase (Pfam/SMART) and UniProt. WD40:  
780 WD40 repeats; CC: coiled-coil domain; Hs1/Cortactin: Hs1/Cortactin repeats; SH3: SH3 domain; PRD:  
781 proline rich domain; WCA: WH2/verprolin, cofilin, acidic domains; LRR: Leucine-rich repeats; PH: pleckstrin  
782 homology domain; LLR: Leucine-rich repeats; C-terminal: Carmil c-terminal domain; DUF: domains of  
783 unknown function. Domain size is not to scale. (B) Cycle 11 apical actin cap area dynamics in control,  
784 Arp2/3, and ANRP disrupted embryos: control (black, n=15, N=4), *DPod1 shRNA* (green, n=11, N=3),  
785 *Coronin shRNA* (blue, n=9, N=3), *Cortactin shRNA* (red, n=12, N=3), *Scar shRNA* (orange, n=11, N=3),  
786 *Carmil shRNA* (grey, n=9, N=3), and ArpC4 shRNA (magenta, n=11, N=3). Cap areas are normalized to  
787 the size at t=0s. (C, D, F, H, J, L) Still images from live-imaging of apical F-actin dynamics  
788 (UAS:moeABD:mCh, cycle 11) at t=180, 270, 360s, from control (C), *DPod1 shRNA* (D), *Coronin shRNA*  
789 (F), *Cortactin shRNA* (H), *Scar shRNA* (J), and *Carmil shRNA* (L) embryos. Images are identically leveled  
790 and imaged. Scale bar=5µm. (E,G,I,K,M) Apical actin cap area dynamics (cycle 11) in control (black, n=15,  
791 N=4), *DPod1 shRNA* (green, n=11, N=3), *Coronin shRNA* (blue, n=9, N=3), *Cortactin shRNA* (red, n=12,  
792 N=3), *Scar shRNA* (orange, n=11, N=3), *Carmil shRNA* (grey, n=9, N=3), and ArpC4 shRNA (magenta,  
793 n=11, N=3). Cap areas are normalized to the size at t=0s. (E',G',I',K',M') Absolute actin cap areas (µm<sup>2</sup>) in  
794 control and ANRP compromised embryos from cycle 11 at indicated time points. \*: p<0.05. (E'',G'',I'',K'',M'')  
795 Actin cap average intensity in control and ANRP compromised embryos from cycle 11 at indicated time  
796 points. \*: p<0.05. Bar graphs without \* labeled in (E'-E'',G'-G'',I'-I'',K'-K'',M'-M'') are not significant. (N) Still  
797 images of endogenous CRISPR Arp3:GFP behavior in control and actin regulator disrupted embryos at  
798 t=120s in cycle 11. Scale bar=5µm. (O) CRISPR Arp3:GFP intensity in control and different actin regulators  
799 functional disruption embryos at t=120s in cycle 11. control: n=13, N=3; ArpC4 shRNA: n=18, N=3; *DPod1*  
800 *shRNA*: n=34, N=3; *Coronin shRNA*: n=30, N=3; *Scar shRNA*: n=24, N=3; *Cortactin shRNA*: n=27, N=3;  
801 *Dia shRNA*: n=28, N=3. ns: not significant, \*: p<0.05, \*\*: p<0.005; \*\*\*: p<0.0005.

802

**Figure 4**

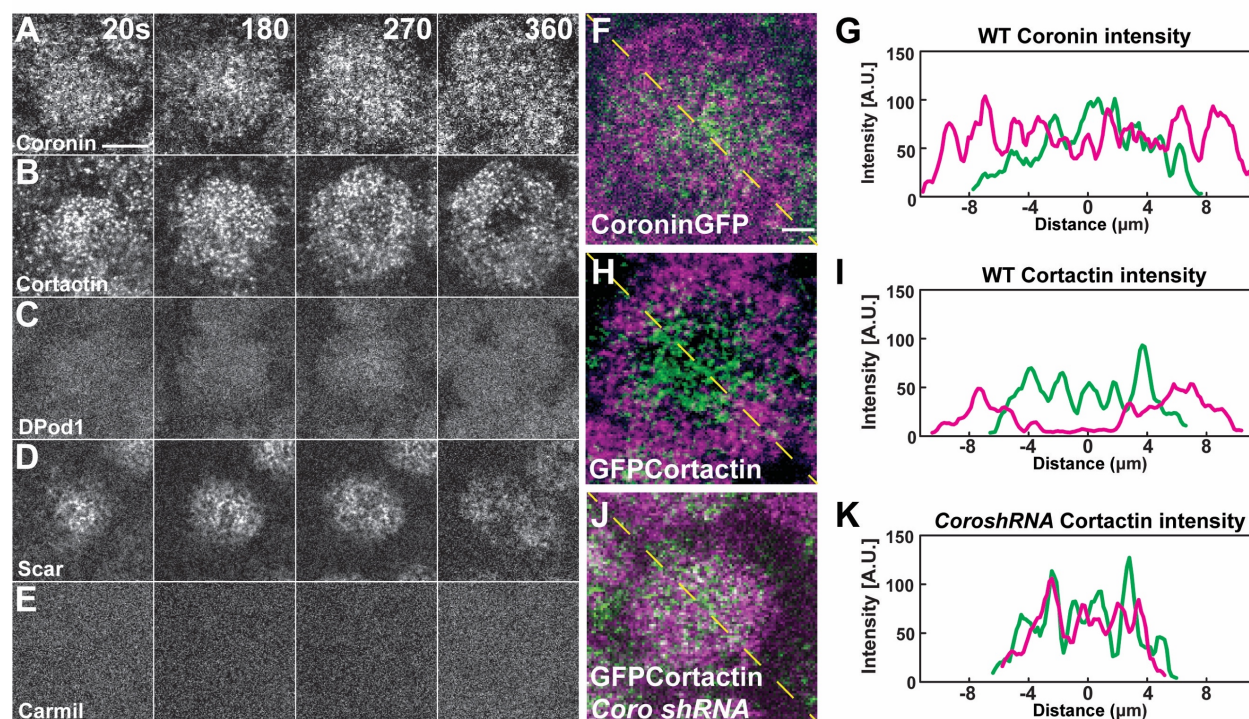


**Figure 4. ANRP localization at apical actin caps.** (A-E) Coronin (UAS:Coronin:GFP), Cortactin (UAS:GFP:Cortactin), DPod1 (UAS:DPod1:GFP), Scar (UAS:Scar:GFP), and Carmil (UAS:Carmil:GFP) localization on apical cap structures at t=20, 180, 270, and 360s. *Additional Cortactin CRISPR and DPod1 CRISPR allele and anti-Coronin immunostaining data in Fig. S6.* Scale bar=5 $\mu$ m. (F-H) Cortactin transitions to actin periphery through Coronin antagonism during cap growth. Overlapped images from t=360s (magenta) to t=180s (green) from live-imaging. Coronin (F) and Cortactin (H) images are derived from live-imaging of UAS:Coronin:GFP (F) and CRISPR GFP:Cortactin (Fig S6B), respectively. Scale bar=2 $\mu$ m. (J) CRISPR GFP:Cortactin t=180s (green) and 360s (magenta) overlapped images in *Coronin shRNA* disrupted embryo. Scale bar=2 $\mu$ m. (G, I, K) Intensity profiles from (F), (H), and (J) yellow lines, respectively. Distance=0 $\mu$ m indicates the center of apical cap structures.

**Figure 5**

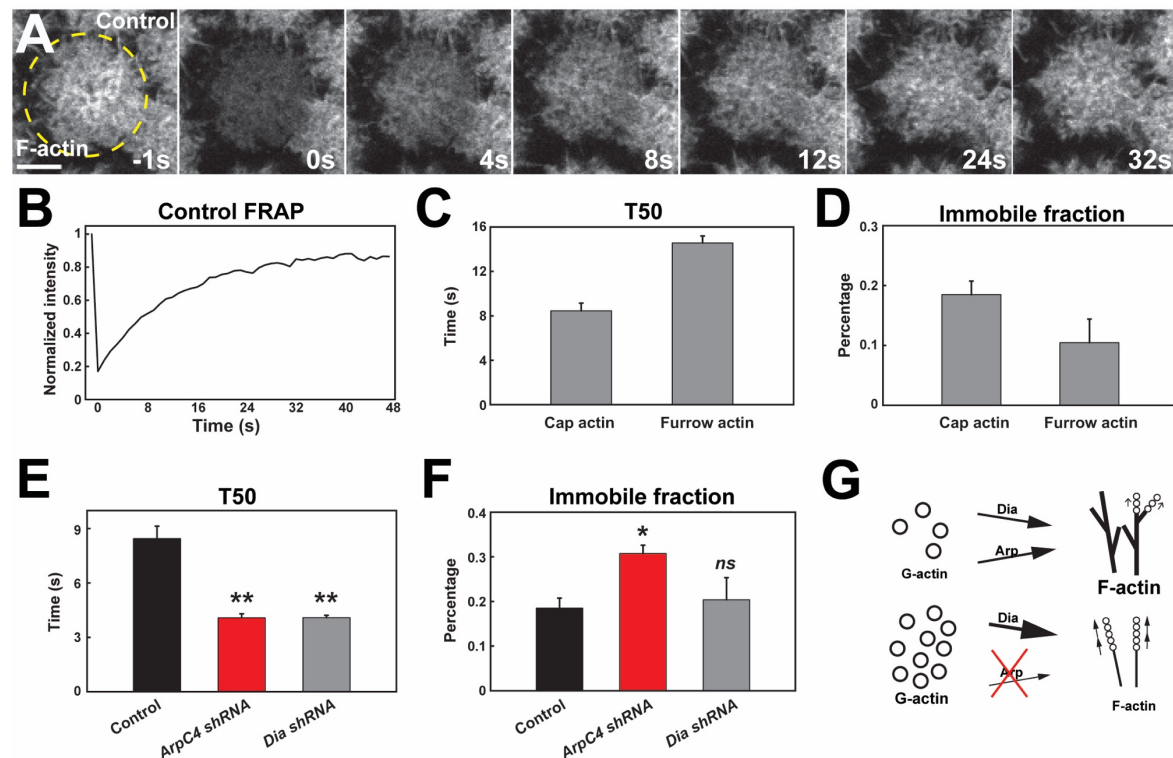
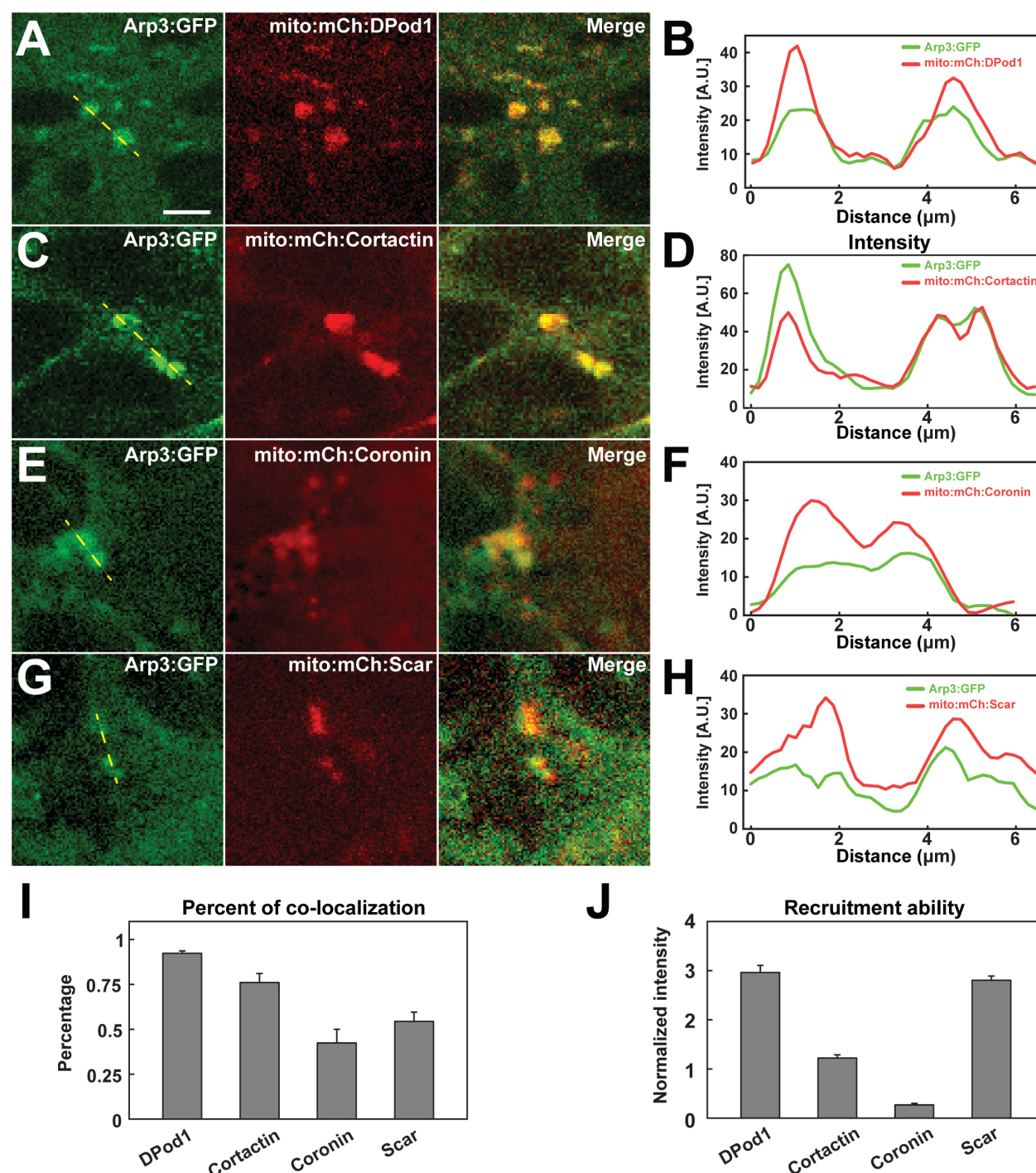


**Figure 5. Arp2/3 and Formin network analysis suggests competition for free G-actin.** (A) Still images from FRAP recovery of F-actin live-imaging (UAS:moeABD:mCh) in cycle 11 embryos at t=-1s (1 second before photo bleaching), 0s (photo bleaching), 4s, 8s, 12s, 24s, and 32s. Scale bar=5μm. (B) FRAP recovery dynamics in control apical actin cap at cycle 11. Intensity is normalized to the value at t=-1s. (C-D) FRAP T50 and immobile fraction of F-actin at apical cap (n=6) and furrow (n=3) structures in cycle 11. (E-F) FRAP T50 and immobile fraction of F-actin at apical cap structures from control (n=6), *ArpC4 shRNA* (n=4), and *Dia shRNA* (n=4) in cycle 11 embryos showing faster actin recovery rates in *ArpC4* and *Dia* shRNA embryos. ns: not significant, \*: p<0.05, \*\*: p<0.005. (G) Schematic of Arp2/3 and Dia competition for limited G-actin pool.



**Figure 6**



842 DPod1, Cortactin, Coronin and Scar. DPod1: n=26, N=3; Cortactin: n=29, N=3; Coronin: n=27, N=4; Scar:  
843 n=40, N=3.  
844



**Figure 7**

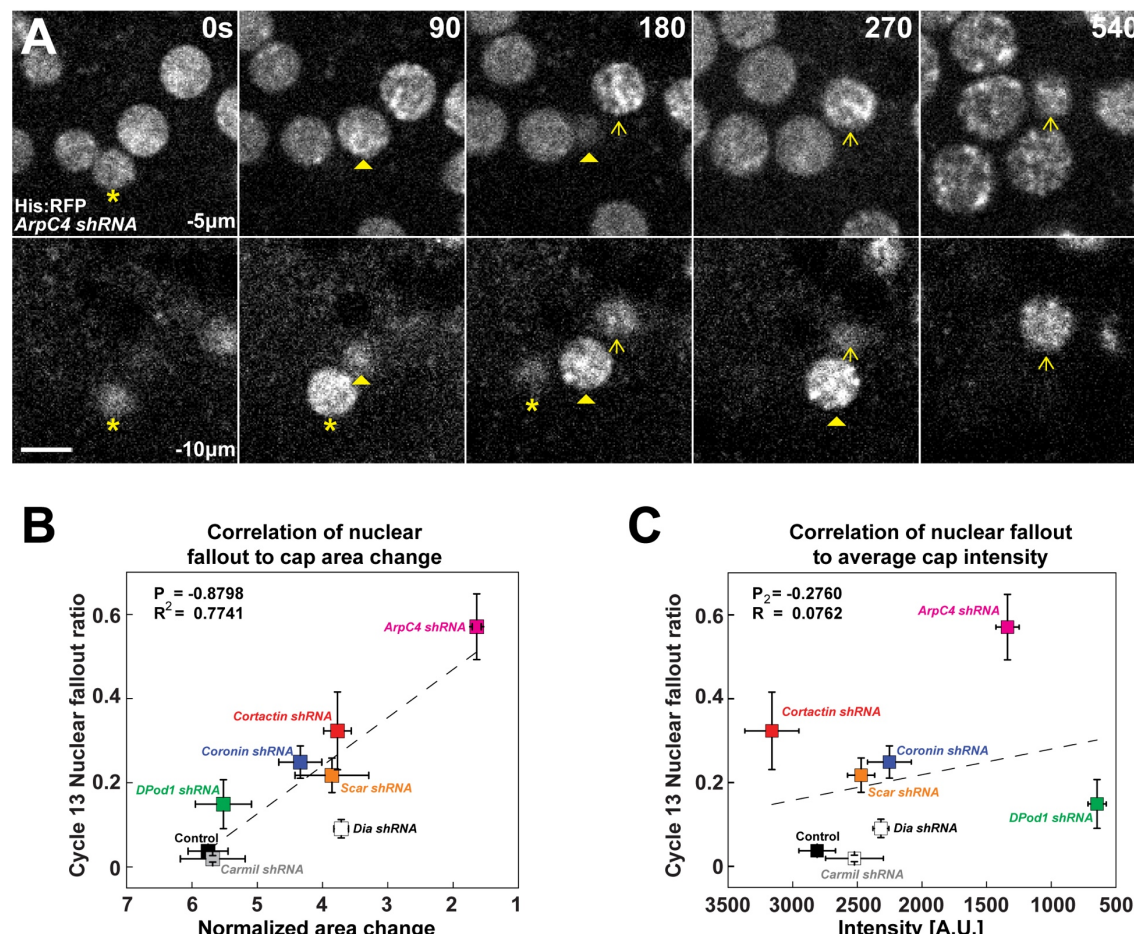


**Figure 7. Requirement for filamentous actin cap ANRP function in anchoring embryonic nuclei.** (A) Nuclei (marked by Histone:RFP) lose apical anchorage and fall into the embryonic interior in *ArpC4 shRNA* embryos during cycle 12 at t=0s, 90s, 180s, 270s and 540s. Medial z-layer (-5μm from apical most portion of embryo) indicates plane of normal nuclear positioning, and basal layer (-10μm) images are shown. Asterisk, arrowhead and arrow indicate individual falling-out nuclei. Scale bar=5μm. (B) Correlation of nuclear fallout rates to cap area expansion rates (t=0-120s) in indicated backgrounds (cycle 13 embryos). (C) Correlation of nuclear fallout rates to average actin cap intensities (t=120s) in indicated backgrounds (cycle 13 embryos). (B,C) control (n>12, N>3), *Dia shRNA* (n=10, N=3), *ArpC4 shRNA* (n=11, N=3), *DPod1 shRNA* (n=11, N=3), *Coronin shRNA* (n=9, N=3), *Cortactin shRNA* (n=12, N=3), *Scar shRNA* (n=11, N=3), and *Carmil shRNA* (n=9, N=3). Dashed lines indicate linear regression fitting. P: Pearson's correlation coefficient, R<sup>2</sup>: coefficient of determination.

# SUPPLEMENT

**Table 1: Arp2/3 and ANRPs toolkit**

Construct	Vector	Chromosome
CRISPR Arp3:GFP	Endogenous	III
CRISPR GFP:Cortactin	Endogenous	III
CRISPR GFP:DPod1	Endogenous	X
UAS:GFP:Cortactin	pUAST	X, II, III
UAS:Cortactin:GFP	pUAST,pUAS p	X, II, III
UAS:mCherry:Cortactin	pUASp	II, III
UAS:DPod1:GFP	pUAST	X, II, III
UAS:Coronin:GFP	pUAST	II, III
UAS:GFP:Carmil FL	pUAST	X, II, III
UAS:Carmil FL:GFP	pUAST	X, II, III
UAS:Scar:GFP	pUASp	II, III
UAS:mito:mCherry:Cortactin	pUASp	II, III
UAS:mito:mCherry:Coronin	pUASp	X, II, III
UAS:mito:mCherry:DPod1	pUASp	II, III
UAS:mito:mCherry:Scar	pUASp	II, III

**Table 2: Stocks and genetics**

Stocks	Source	Identifier
<b>General stocks</b>		
P[mat-tub-Gal4] mat67	D. St Johnston	
P[mat-tub-Gal4] mat15	D. St Johnston	
UAS:mCherry:MoesinABD	T. Millard	
Histone:RFP	BDSC	BDSC 23650 III; BDSC 23651 II
UAS:GFP:Act88F	BDSC	BDSC #9253
Wasp:sGFP	VDRC	VDRC #318474
Wash:GFP	BDSC	BDSC #81644
YFP:mito	BDSC	BDSC #7194
UAS:mCh:mitoOMM	BDSC	BDSC #66532, 66533

nos-Cas9	Bestgene	NIG-FLY #CAS-0001, CAS-0003
w1118	Bestgene	
<b>shRNA (Valium) lines</b>		
<i>ArpC4 shRNA</i>	DRSC/TRiP	BDSC #41888
<i>Dia shRNA</i>	DRSC/TRiP	BDSC #35479
<i>DPod1 shRNA</i>	DRSC/TRiP	BDSC #41705
<i>Coronin shRNA</i>	DRSC/TRiP	BDSC #40841
<i>Cortactin shRNA</i>	DRSC/TRiP	BDSC #44425
<i>Carmil shRNA</i>	DRSC/TRiP	BDSC #41686
<i>Scar shRNA</i>	DRSC/TRiP	BDSC #51803
<i>Wasp shRNA</i>	DRSC/TRiP	BDSC #51802
<i>Wash shRNA</i>	DRSC/TRiP	BDSC #62866

867

868

869 **Table 3: Reagents**

Reagent	Source	Identifier
<b>Antibodies and dyes</b>		
Rabbit anti-GFP	Invitrogen	A11122
Mouse anti-dsRed	Clontech	632393
Alexa Fluor Goat anti rabbit 488	Invitrogen	A11034
Alexa Fluor Goat anti mouse 568	Invitrogen	A11031
Alexa 568-Phalloidin	Invitrogen	Cat# A12380
Alexa 647-Phalloidin	Invitrogen	Cat# A22287
<b>Chemicals and kits</b>		
Halocarbon oil 27		Cat# H8773
Halocarbon oil 700		Cat# H8898
Paraformaldehyde	Electron Microscopy Sciences	Cat# 15714
ProLong Gold	Invitrogen	Cat# P36931
Jasplakinolide	Santa Cruz Biotech	Cat# sc-202191
Latrunculin B	Sigma	Cat# L5288
QIASHredder	QIAGEN	Cat# 79654

Quick-RNA MicroPrep	Zymo Research	Cat# R1050
QuantiTech Reverse Transcription Kit	QIAGEN	Cat# 205310
QuantiTech SYBR Green RT-PCR	QIAGEN	Cat# 204141
Q5 site-directed mutagenesis	NEB	Cat# E0554S
EZNA insect DNA kit	Omega bio-tek	Cat# D0926-01
<b>Software</b>		
iQ5	Bio-Rad	bio-rad.com
FIJI/ImageJ	(Schneider et al., 2012)	Fiji.sc
Micromanager 1.4	(Edelstein et al., 2014)	micro-manager.org
OriginPro	OriginLab	originlab.com
Photoshop	Adobe	adobe.com
Illustrator	Adobe	adobe.com
<b>Peptides and oligonucleotides</b>		
Coronin peptide for antibody	GenScript	CLPAKKAGNILNKPR
TOM70-HA	S. Munro lab	
<b>qPCR primers</b>		
Sqh(MRLC)	QuantiTect	Cat# QT00499065
Rh3	QuantiTect	Cat# QT00978481
DPod1 set1	QuantiTect	Cat# QT00499464
DPod1 set2	Eurofins	5'-TCCTCACCAAGAACCACTGC
	Eurofins	5'-GTGGGTGGGAACAGATCGTC
Coronin set1	QuantiTect	Cat# QT00940737
Coronin set2	Eurofins	5'-ACAGGCTTCAACCGTAGCTC
	Eurofins	5'-GAACATTACGCCGTTGGACG
Cortactin set1	QuantiTect	Cat# QT00979020
Cortactin set2	Eurofins	5'-TTCGGAGTGCAAGAGGATCG
	Eurofins	5'-GCACTCCAAATTTGCCTCCG
Arp14D	QuantiTect	Cat# QT00923419
ArpC1(sop2)	QuantiTect	Cat# QT00936222
Dia set1	QuantiTect	Cat# QT00939477
Dia set2	Eurofins	5'-CAAATCGAAGGAGGAGCGACA

	Eurofins	5'-CCCATTCTGCAGGTATTCCAC
Wasp set1	QuantiTect	Cat# QT00984641
Wasp set2	Eurofins	5-ATGGCATGGAGGTGGTCAAG
	Eurofins	5-TTACGCGTCTCTATGGTGGC
Scar set1	QuantiTect	Cat# QT00934584
Scar set2	Eurofins	5'-ACGATCCATAGAACCCGTGC
	Eurofins	5'-GGCGAATGATGTTTCGTCAGC
Carmil set1	Eurofins	5'-CCACTGGTGGGTCGTAAGTC
	Eurofins	5'-GGCATAGACGTCTCCTCAGC
Carmil set2	Eurofins	5'-GCTGAGGAGACGTCTATGCC
	Eurofins	5'-ATAACACTACCCTCGCCTGC
Wash	Eurofins	5'-GCGTAGGAAGAGTGTGGGAC
	Eurofins	5'-GTGATGGAATTGCGCTCGTC
<b>Guide RNAs for CRISPR</b>		
Arp3:GFP		
chiRNA1	Eurofins	5'- CTTCGCTATCAGGTGTGTCACACGA
	Eurofins	5'- AAACTCGTGTGACACACCTGATAGC
chiRNA2	Eurofins	5'- CTTCGCCAGTTCAACCCCCTATCTA
	Eurofins	5'- AAACTAGATAGGGGGTTGAACTGGC
GFP:Cortactin		
chiRNA1	Eurofins	5'- CTTCGGGGCCGACAAAGCCGGATC
	Eurofins	5'- AAACGATCCGGCTTTGTCTGGCCCC
chiRNA2	Eurofins	5'-CTTCGGTGGCCTGAATCTGGTGAC
	Eurofins	5'-AAACGTCACCAGATTCAGGCCACC
GFP:DPod1		
chiRNA1	Eurofins	5'- CTTCGAGCGACTGAGAGGGAGCCAC
	Eurofins	5'- AAACGTGGCTCCCTCTCAGTCGCTC
chiRNA2	Eurofins	5'- CTTCGCGATGTTGTTACCGTACGTC
	Eurofins	5'- AAACGACGTACGGTAACAACATCGC

DPod1 mutated PAM sites in homologous constructs	This study	5'-CCACCGGACTAGTGACACTCGAC 5'-GCAGCGCACAACTGACACTCGAC
	This study	5'-GTGGGCAGCTACCAGACGTACGG
		5'-GTGGGCAGTTATCAACCTATGG

870

# SUPPLEMENTAL FIGURES & FIGURE LEGENDS

## Figure S1

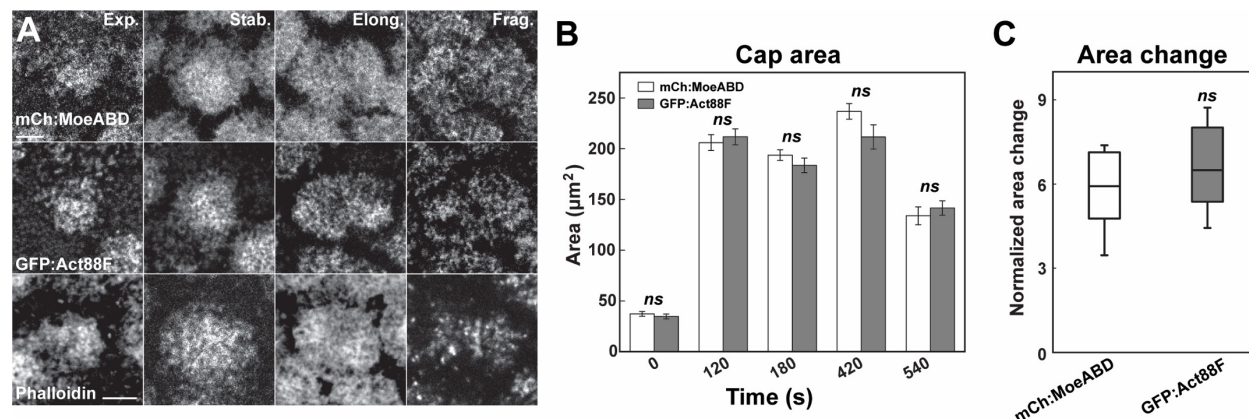
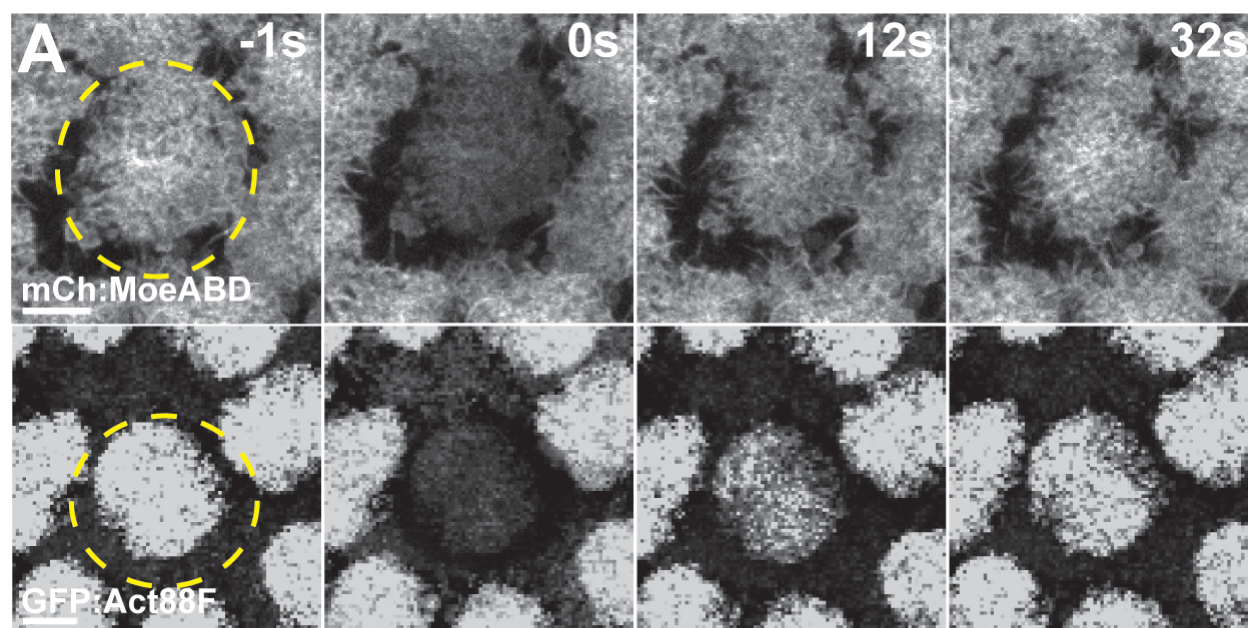


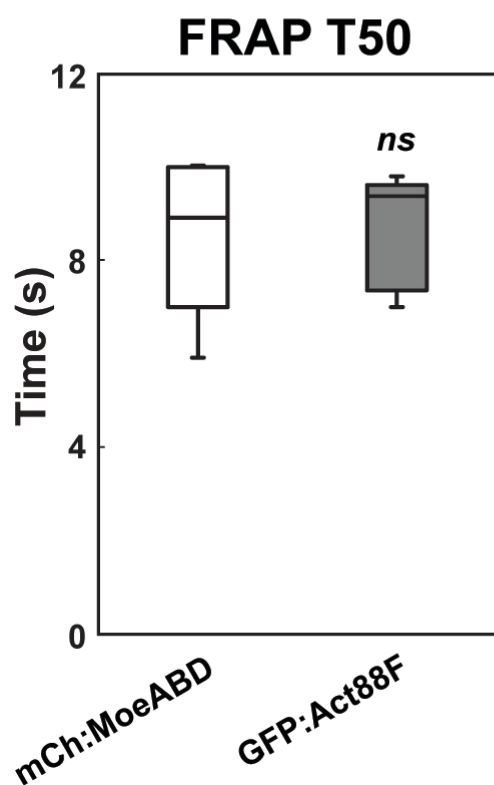
**Figure S1. Similar actin labeling with different actin markers.** (A) Representative images from live-imaged mCh:MoesinABD (actin binding domain of Moesin labeled with mCherry), live-imaged GFP:Act88F (Actin directly labeled with GFP) live-imaging, and fixed Phalloidin staining. *Exponential* (Exp.), *stabilization* (Stab.), *elongation* (Elong.), and *fragmentation* (Frag.) phases are shown. Scale bar=5 $\mu\text{m}$ . (B) Cap area comparison of mCh:MoeABD (n=15, N=4) and GFP:Act88F (n=10, N=3) at t=0, 120, 180, 420, 540s. ns: not significant. (C) Normalized cap area change of mCh:MoeABD (n=15, N=4) and GFP:Act88F (n=10, N=3) at 120s.



**Figure S2**



**B**



**C**

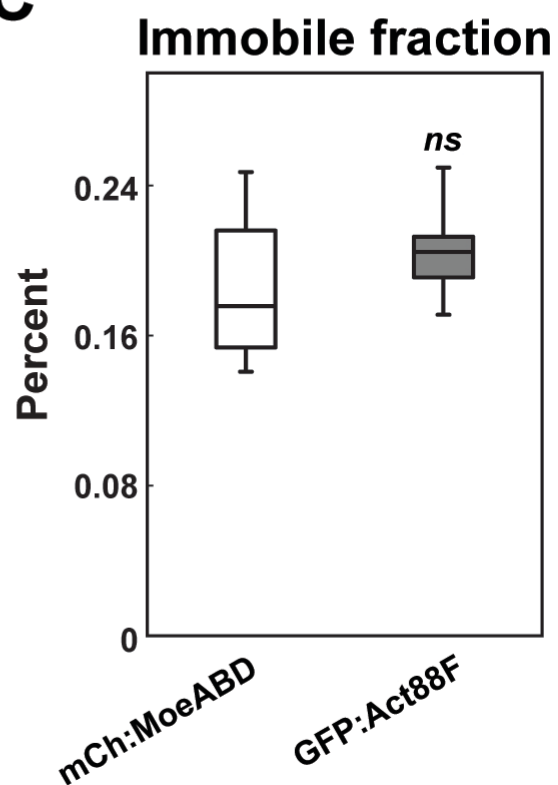


**Figure S2. Similar fluorescent recovery after bleaching (FRAP) actin dynamics with different actin labeling markers.** (A) Representative FRAP images from mCh:MoesinABD and GFP:Act88F at  $t=-1$ s (one second before photo-bleaching), 0s (photo-bleaching), 12s, and 32s in cycle 11 caps during stabilization



888 phase. Scale bar=5 $\mu$ m. (B-C) FRAP T50 and immobile fraction of different F-actin markers: mch:MoeABD  
 889 (n=6) and GFP:Act88F (n=7) structures in cycle 11 caps during stabilization phase.  
 890

# Figure S3

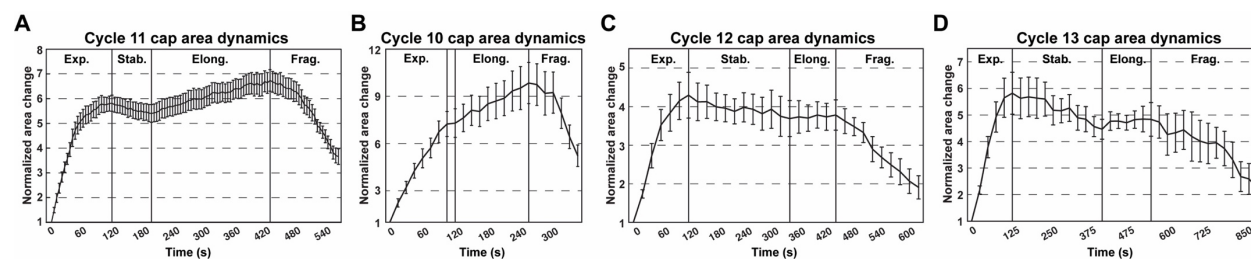


**Figure S3. WT area dynamics of cortical actin caps in cycle 10-13.** (A) Cycle 11 actin cap area dynamics (n=15, N=4) as the standard for analysis. n=15, N=4. Cap areas are normalized to the size at t=0s. Four different phases are labeled (Exp.: *Expansion*; Stab.: *Stabilization*; Elong.: *Elongation*; and Frag.: *Fragmentation* phases). (B-D) Cycle 10, cycle 12 and cycle 13 actin cap area dynamics. Cycle 10: n=6, N=2, measured every 15s; cycle 12: n=6, N=2, measured every 20s; cycle 13: n=6, N=2, measured every 25s. Cap areas are normalized to t=0s at each cycle.

**Figure S4**

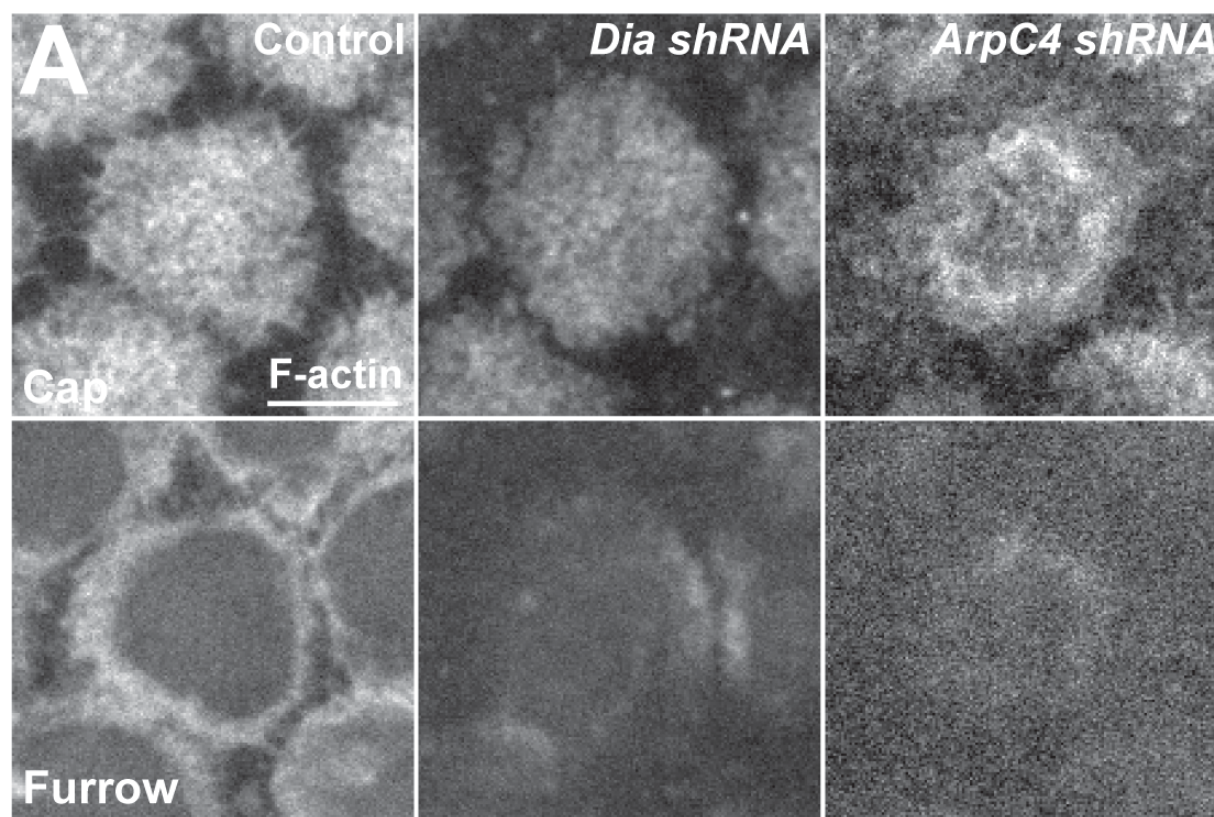


**Figure S4. Apical and furrow-associated actin populations in *Dia* or *Arp2/3* compromised embryos.** (A) Cycle 11 apical cap and furrow actin distributions in Control, *Dia shRNA* and *ArpC4 shRNA* embryos at t=120s. Scale bar=5μm. Cap (0.9μm below apical most layer) and furrow level (3.9μm below apical most layer).

# Figure S5

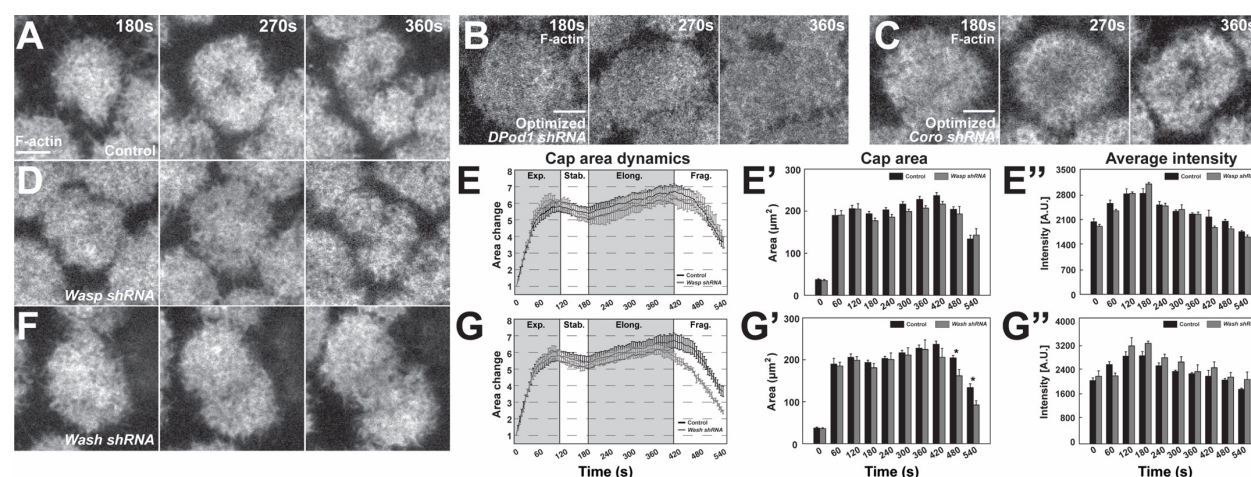


**Figure S5. ANRPs have distinct roles in building apical actin structures.** (A, B, C) Still images from live-imaging of apical F-actin dynamics in cycle 11 at t=180, 270, 360s, from control (A), *DPod1 shRNA* (B), *Coronin shRNA* (C). Images of (B) and (C) are the same images from Figure 3D and 3F but leveled optimally for visualization. Scale bar=5μm. (D, F) Still images from live-imaging of apical F-actin dynamics in cycle 11 at t=180, 270, 360s from control (A), *Wasp shRNA* (D), and *Wash shRNA* (F). Images are identically leveled and imaged as (A). Scale bar=5μm. (E, G) Apical actin cap area dynamics (cycle 11) in control (black, n=15, N=4), *wasp shRNA* (grey, n=11, N=3), and *wash shRNA* (grey, n=9, N=3), respectively. Cap areas are normalized to the size at t=0s. (E', G') Absolute actin cap areas (μm<sup>2</sup>) in control, Wasp and Wash compromised embryos from cycle 11 at indicated time points. (E'', G'') Actin cap average intensity in control and ANRP compromised embryos from cycle 11 at indicated time points. \*: p<0.05. Bar graphs without \* labeled in (E'-E'', G'-G'') are not significant.



**Figure S6**

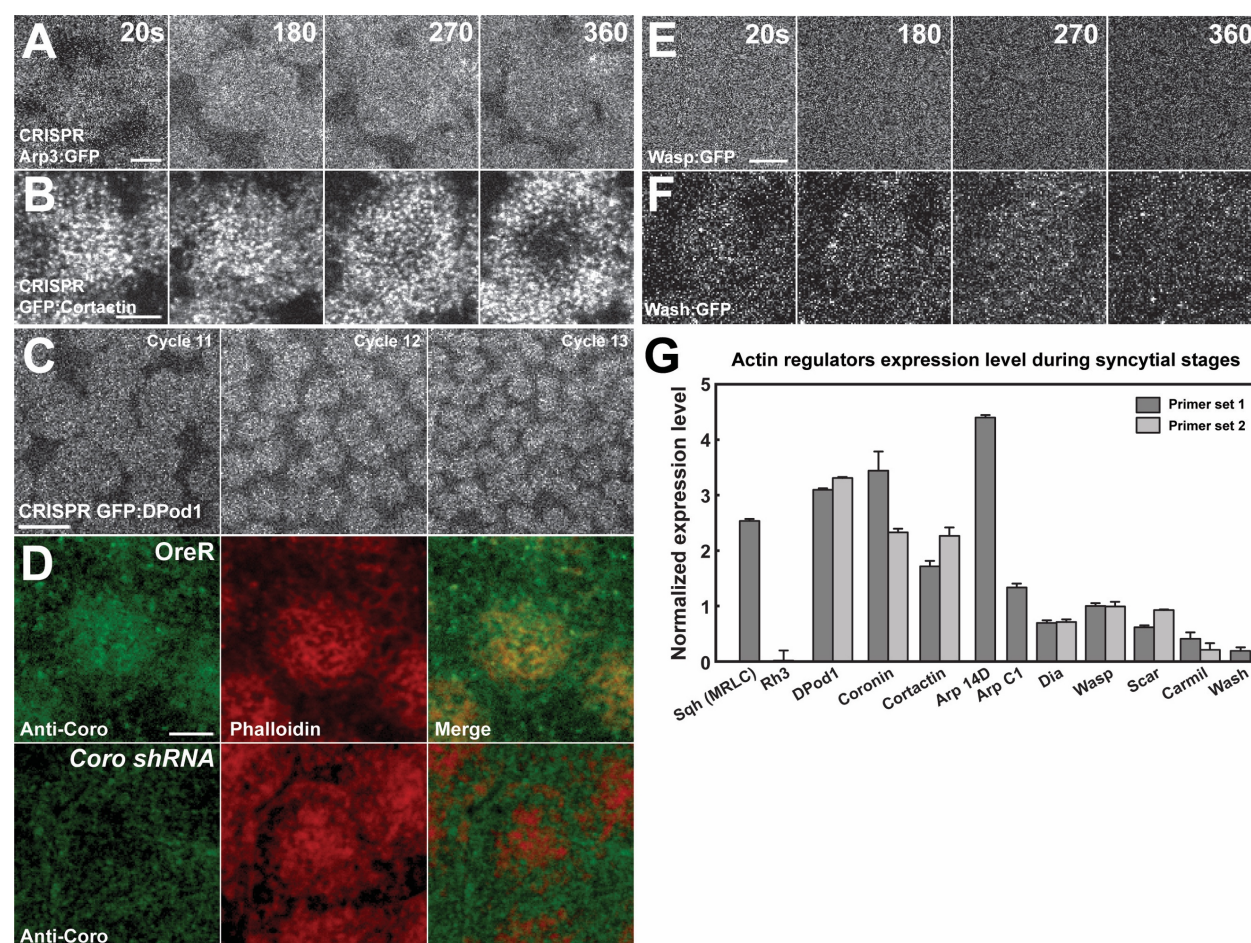


**Figure S6. Expression levels and endogenous localization data of ANRPs.**

(A, B) Still images from live-imaging of apical CRISPR Arp3:GFP (A) and CRISPR GFP:Cortactin (B) in cycle 11 at t=20, 180, 270, 360s. Scale bar=3μm. (C) Still images from live-imaging of apical CRISPR GFP:DPod1 in cycles 11 to 13. Scale bar=10μm. (D) Anti-Coronin (peptide antibody) staining of OreR (WT) and *Coronin shRNA* embryos in cycle 11 with phalloidin staining and merged channels. (E, F) Still images from live-imaging of apical Wasp:GFP (E) and Wash:GFP (F) in cycle 11 at t=20, 180, 270, 360s. Scale bar=3μm. (G) Actin regulators expression level during syncytial cycles by qPCR. Sqh (Myosin II regulatory light chain, MRLC) as positive control, and Rh3 (Rhodopsin 3) as negative control. The data are normalized to Wasp. DPod1, Coronin, Dia, Wasp, Scar and Carmil are tested by two independent sets of primers.

# Figure S7

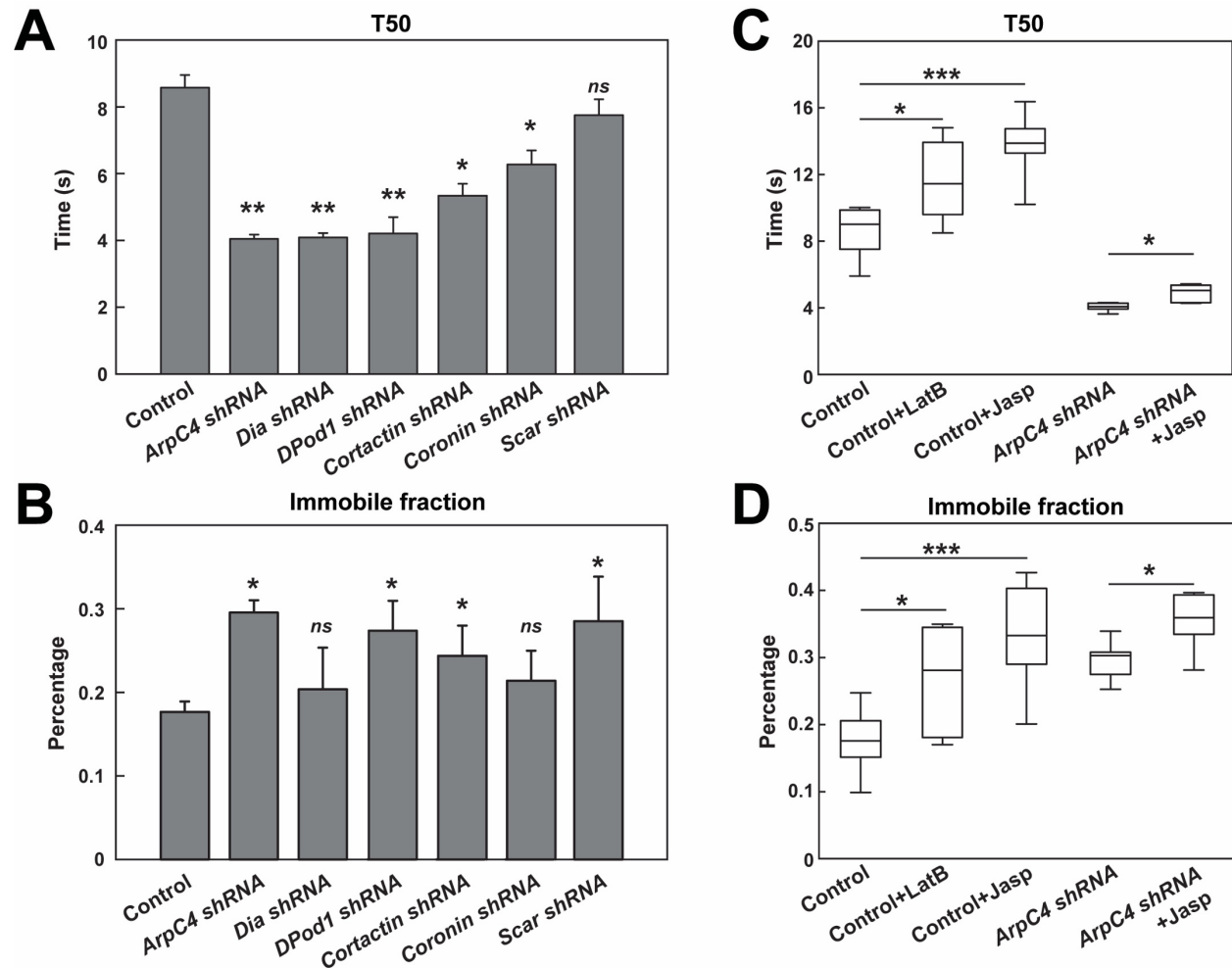


**Figure S7. FRAP on Arp2/3 and ANRPs disrupted embryos.** (A-B) FRAP T50 and immobile fraction of F-actin in control and indicated actin regulator compromised embryos in cycle 11.  $n > 3$ . *ns*: not significant, \*:  $p < 0.05$ . (C-D) FRAP T50 and immobile fraction of F-actin in control ( $n = 13$ ), Latrunculin B (LatB) ( $n = 5$ ) and Jasplakinolide (Jasp) injected embryos ( $n = 8$ ), or performed in *ArpC4* shRNA embryos ( $n = 5$ ) and *ArpC4* shRNA with Jasp injection ( $n = 5$ ). \*:  $p < 0.05$ , \*\*\*:  $p < 0.0005$ .

**Figure S8**

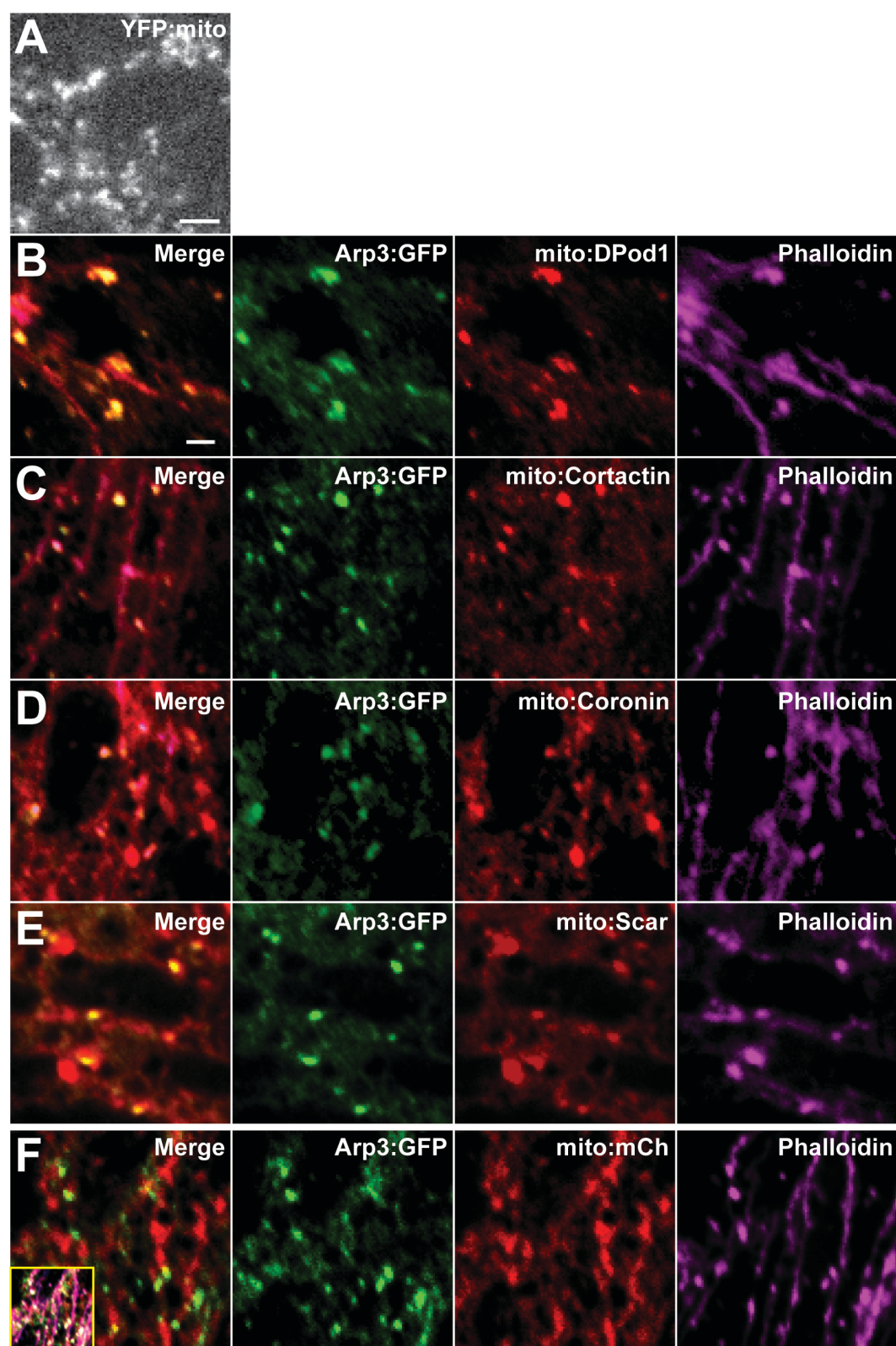


**Figure S8. Mito-tagged ANRPs can direct F-actin polymerization.** (A) Still images of mitochondrial morphology from YFP:mito in stage 12 embryo. Scale bar=1 $\mu$ m. (B-E) Staining images of CRISPR Arp3:GFP (anti-GFP) with mito-tagged mCherry:ANRPs (anti-dsRed) and F-actin (Phalloidin) in cells at stage 12. (F) Control staining images of CRISPR Arp3:GFP (anti-GFP) with mCherry-tagged mitochondrial marker (anti-dsRed) and F-actin (Phalloidin) in cells at stage 12. Main merge panel is 2-way merge between Arp3:GFP and mito:mCh, inset is 3-way merge between all channels. Scale bar=1 $\mu$ m.